A mechanistic model for lateral erosion of bedrock channel banks by bedload particle impacts

Tingan Li[1*], Theodore K. Fuller[2], Leonard S. Sklar[3], Karen B. Gran[4], and Jeremy G. Venditti[1,5]

[1]Department of Geography, Simon Fraser University, Burnaby, British Columbia, V5A 1S6, Canada

[2]Department of Earth and Environmental Sciences, St. Anthony Falls Laboratory, University of Minnesota, Minneapolis, MN, 55414, United States

[3]Department of Geography, Planning, and Environment, Concordia University, Montreal, Québec, H3G 1M8, Canada

[4]Department of Earth and Environmental Sciences, University of Minnesota, Duluth, MN, 55812, United States

[5]School of Environmental Science, Simon Fraser University, Burnaby, British Columbia, V5A 1S6, Canada

*Corresponding author: Tingan Li (Tingan_Li@sfu.ca)

Key Points:

- A mechanistic lateral erosion model for bedrock rivers is developed, based on the abrasion caused by deflected bedload particles
- The undercut wall shape observed in laboratory experiments are successfully reproduced by the lateral erosion model
- Vertical erosion dominates under ~ 75% of sediment transport and supply conditions, but is outpaced by lateral erosion when the bed is near fully covered

Abstract

Bedrock rivers get wider by lateral erosion. Lateral erosion is widely thought to occur when the bed is covered by alluvium, which deflects the downstream transport of bedload particles into channel walls. Here we develop a model for lateral bedrock erosion by bedload particle impacts. The lateral erosion rate is the product of the volume eroded per particle impact and the impact rate on the wall. The volume eroded per particle impact is modelled by tracking the motion of bedload particles from collision with roughness elements to impacts on the wall. The impact rate on the wall is zero if the bedload particle deflected by roughness elements cannot reach the wall. Otherwise, the impact rate on the wall is the same with that on roughness elements. The model further incorporates the co-evolution of wall morphology, shear stress and erosion rate. The model predicts the undercut wall shape observed in physical experiments. The non-dimensional lateral erosion rate is used to explore how lateral erosion varies under different relative sediment supply (ratio of supply to transport capacity) and transport stage conditions. Maximum lateral erosion rates occur at high relative sediment supply rates (~ 0.7) and moderate transport stages (~10). The competition between lateral and vertical erosion is investigated by coupling the saltation-abrasion vertical erosion model with our lateral erosion model. The results suggest that vertical erosion dominates under near 75% of supply and transport stage conditions, but is outpaced by lateral erosion near the threshold for full bed coverage.

1. Introduction

Bedrock river incision sets the pace of landscape evolution in unglaciated landscapes (Willett, 1999; Whipple, 2004). Bedrock rivers are laterally constrained by rock banks and have intermittently exposed rock beds that incise vertically (Turowski et al., 2008a; Meshkova et al., 2012). Bedrock rivers form the lower boundary of hillslopes (Perron et al., 2008) and thus are hard points in the landscape that must be cut through to lower the elevation of the whole landscape (Rennie et al., 2018; Venditti et al., 2019). Incision rates of bedrock rivers are typically modelled as a function of stream power (Seidl & Dietrich, 1992; Anderson, 1994; Tucker & Slingerland, 1994; Willett, 1999; Hancock & Anderson, 2002) or boundary shear stress parametrized from basin slope-area relations (Howard & Kerby, 1983; Howard, 1994; Moglen & Bras, 1995; Stark, 2006; Tucker & Slingerland, 1996; Whipple & Tucker, 1999; Wobus et al., 2006). These models allow for large-scale predictions of landscape evolution over geologic time scales, but mask physical processes responsible for bedrock river incision. This makes them difficult to apply in real landscapes and of little value for reach-scale predictions, where active incision occurs. Process-based models are needed to investigate the relative role of controlling variables such as rock strength, grain size, roughness, water discharge and sediment supply and to provide more detailed physical explanations (Whipple et al., 2000; Whipple, 2004; Sklar & Dietrich, 2004, 2006; Nelson & Seminara, 2011; Huda & Small, 2014; Beer & Turowski, 2015; Turowski, 2018).

Vertical erosion processes are well known and several models exist to represent them. Whipple et al. (2000) summarized the processes of vertical incision: abrasion by sediment impacts of bedload or suspended load; plucking from the bed by hydraulic forces; chemical and physical weathering; cavitation; and debris-flow scour. Detailed models of the physics of individual incision processes have been developed to predict bedrock river dynamics, including: saltation abrasion model (Sklar & Dietrich, 2004); total-load abrasion model (Lamb et al., 2008); plucking model based on the block topple-sliding mechanism (Lamb et al., 2015; Larsen & Lamb, 2016); bedload abrasion, macroabrasion and plucking model (Chatanantavet & Parker, 2009); and weathering model (Hancock et al., 2011). These models have been used to predict how vertical incision in bedrock channels changes in response to changing boundary conditions (Whipple, 2004; Sklar & Dietrich, 2006, 2008; Egholm et al., 2013; Huda & Small, 2014; Larsen & Lamb, 2016).

However, bedrock rivers can also erode laterally, and adjust their width. Undercut walls are evidence of active, local width adjustment (Figure 1). Local variations in bedrock river width can induce highly turbulent plunging flow as water enters the narrow part of bedrock rivers, which can in turn promote erosion of the bed and sidewalls by bedload particle impacts (Venditti et al., 2014). Lateral incision has also been observed to be responsible for formation of strath terraces (Fuller et al., 2009), creation of wide valley bottoms (Snyder & Kammer, 2008) and planation of valley bottoms (Cook et al., 2014) at large scales. Therefore, understanding lateral erosion mechanisms is crucial for exploring bedrock width dynamics and its influence on fluvial processes from local (reach) to large scales. In comparison to what is known about vertical erosion, however, comparatively little is known about lateral erosion mechanisms. Existing lateral erosion models rely on the stream power law to link stream power or parametrized shear stress to erosion rates with various degrees of sophistication (Hancock & Anderson, 2002; Finnegan et al., 2005; Stark, 2006; Wobus et al., 2006; Lague, 2010; Langston & Tucker, 2018; Yanites, 2018). Most of these models ignore

the influence of sediment supply on lateral erosion by simply scaling the lateral erosion rate with shear stress (Stark, 2006; Wobus, 2006) or the rate of energy dissipation per unit area of the channel wall created by centripetal acceleration around a bend (Langston & Tucker, 2018). Others have introduced the influence of alluvial cover on limiting lateral erosion in high sediment supply environments (Hancock & Anderson, 2002; Lague, 2010; Yanites, 2018), but did not include a quantitative relation between sediment supply and lateral erosion rate. Turowski (2019) recently developed a lateral bank erosion model due to bedload particle impacts, deflected by gravel bars. The model does not include the physics of deflections, but rather treats the gravel alternate bars as a source of roughness capable of deflecting particles in an otherwise straight bedrock channel. This produces the counterintuitive result that decreasing lateral erosion rates occur with increasing extent of alluvial cover because gravel bars increase their length as the cover gets greater due to the assumption of constant aspect ratio of gravel bars.

Gilbert (1877) first suggested that a bedrock channel will incise laterally when the channel bed is covered with transient alluvial deposits. Recent research on lateral erosion has focused on the role of sediment supply on setting the relative rates of vertical and lateral erosion (Turowski et al., 2007; Fuller et al., 2009; Finnegan & Balco, 2013). These investigations suggest lateral erosion dominates in high sediment supply environments, but is limited in low sediment supply environments. None of these studies propose a specific process or mechanism to explain how the high sediment supply drives lateral erosion. Physical experiments have documented channel widening by bedload abrasion (Finnegan et al., 2007; Johnson & Whipple, 2010). Enlighted by these experiments, Fuller et al. (2016) further explored the erosional mechanism of deflection of saltating bedload particles into the channel wall by roughness elements, and concluded that it is an effective mechanism for lateral erosion into bedrock. This mechanism explains why lateral erosion dominates in high sediment supply environments where intermittent alluvial cover likely occurs. The downstream transport of bedload particles is deflected by alluvial cover and obtain lateral momentum to erode the wall. In low sediment supply environments, alluvial cover may not be available to deflect bedload particles. This newly identified mechanism for lateral erosion opens the door for a mechanistically-based lateral erosion model.

Here we develop a mechanistic model to explore the potential efficacy of bedload particle impacts as a mechanism of lateral erosion in bedrock channels and test the model using the Fuller et al. (2016) flume experiments, referred to as Fuller Experiments hereafter. Our model only considers the collision between bedload particles and bed roughness elements as the sole process by which saltating bedload particles obtain lateral momentum to erode the wall. The model is formulated by determining the initial velocity of bedload particles before collision with bed roughness elements from empirical relations (Sklar & Dietrich, 2004), estimating the momentum transfer during collision from a simplified reflection methodology, and tracking the movement of bedload particles from collision with bed roughness elements to impact on the wall using force balance equations. This allows the distribution of lateral erosion on the wall to be calculated. The model is implemented with and without co-evolution of wall morphology, shear stress, and erosion rate to explore how channel change influences the results. The lateral erosion model is coupled with the Sklar & Dietrich (2004) vertical incision model to investigate the competition between vertical and lateral erosion with transport stage and relative sediment supply.

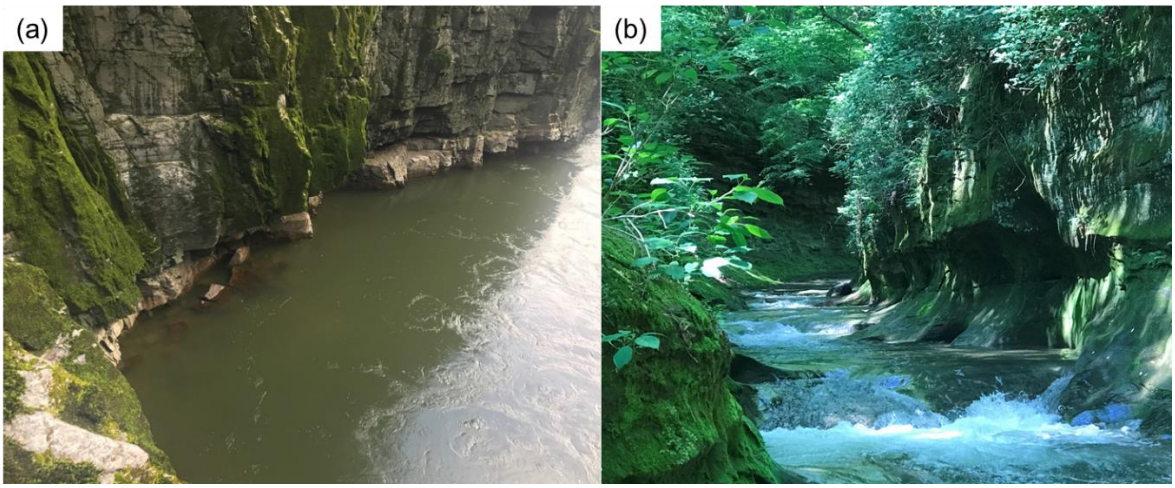

Figure 1 Examples of undercut walls in a) Fraser Canyon, British Columbia. b) Fall Creek Gorge, Indiana.

2. Model Development

The model is based on the saltation-abrasion mechanism of bedrock erosion and the well-known tools and cover effect (Sklar & Dietrich, 2004). Erosion rates are a function of sediment supply, transport stage, grain size and rock strength (Sklar & Dietrich, 2004; 2008). When the bed is relatively free of cover, impacts of saltating bedload particles are capable of detaching rock particles from the surface. Vertical erosion is limited at high sediment supply rates, when the bed is covered. However, when covered, downstream transport of saltating bedload particles can be deflected by bed roughness elements and directed towards channel walls, which induces lateral erosion. Following the saltation-abrasion vertical erosion model formulation (Sklar & Dietrich, 2004), we assume that the flow, sediment transport and distribution of roughness elements are uniform in a bedrock channel with a planar bed and straight walls. We use a hybrid approach to model lateral erosion by impacts of saltation bedload particles. First, we model all the possible individual deflection trajectories from discrete parts of the roughness elements for a given hydraulic condition. Then we apply these results in a continuum model by calculating the deflection rates on each cell of the roughness surface and calculate the resultant erosion rates as a function of locations on the wall.

2.1 Initial hydraulic, flow resistance and bedload transport conditions

We assume that bed roughness elements are composed of immobile semi-spheres with diameter of D_r and an areal fraction of F_r, arranged in uniformly distributed rows and columns with a spacing of d (Figure 2). Initial hydraulic conditions are calculated from six input variables: water discharge Q_w, channel width W, channel slope S, roughness element diameter D_r, areal fraction F_r of roughness elements and bedload particle diameter D.

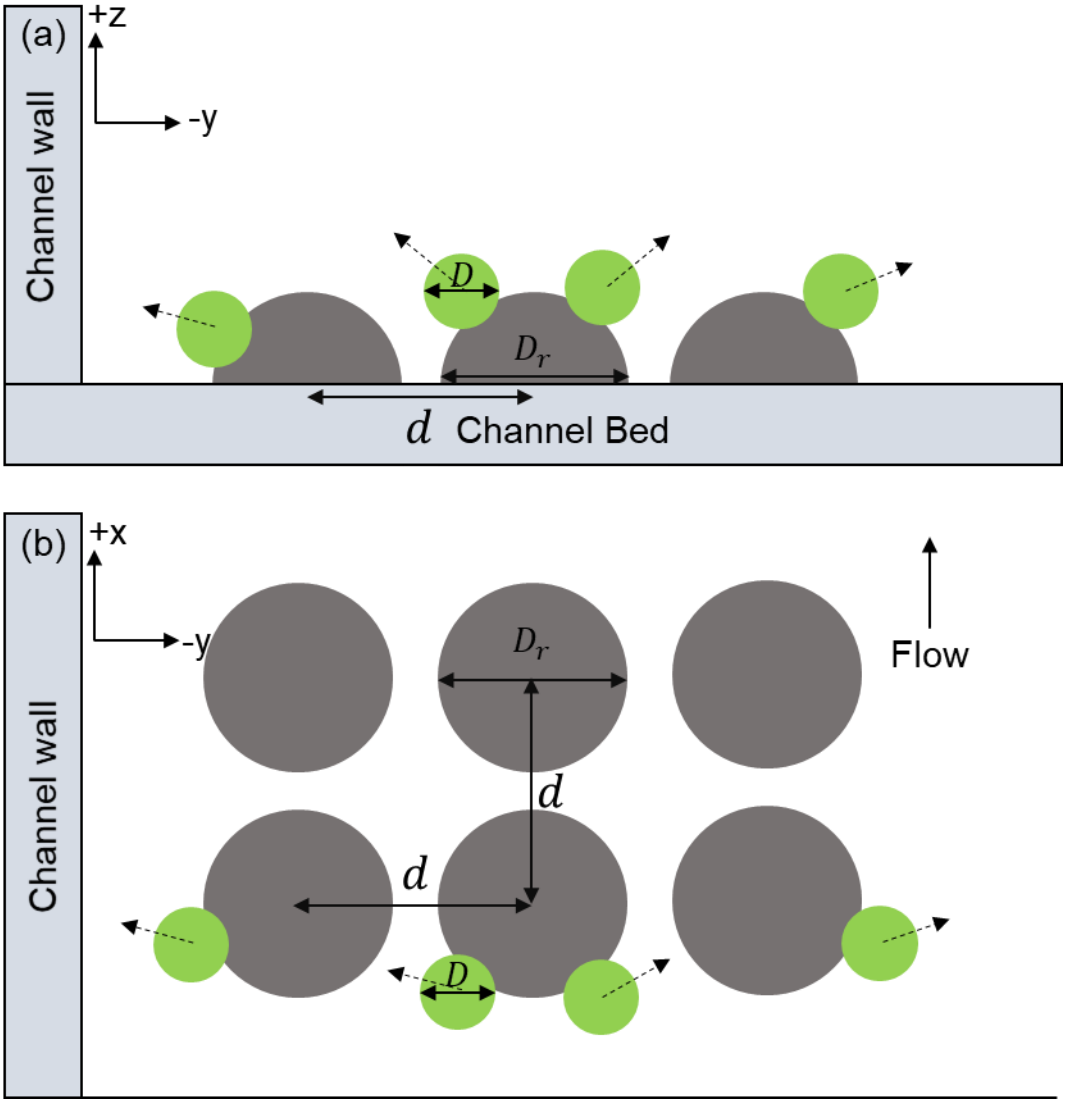

Figure 2 a) Cross section view and b) plan view of model setup in an idealized rectangular channel eroded by saltating bedload particles that are deflected by roughness elements distributed on the channel bed. The grey semi-spheres represent roughness elements with diameter of D_r, which are equally distributed in rows and columns with the same distance d. The green spheres represent bedload particles that impact roughness elements. Only one side of the channel walls is shown here and used for simulation, assuming the walls are symmetrical.

Asumming steady uniform flow, the total shear stress τ is given as

$$\tau = \rho_w g h S \quad (1)$$

where ρ_w is water density, g is gravity acceleration, h is water depth.
τ can also be expressed as a function of Darcy-Weisbach hydraulic friction factor f and mean flow velocity U

$$\tau = \frac{\rho_w f U^2}{8} \quad (2)$$

In a bedrock channel with roughness elements and transported bedload particles, the flow resistance is derived from the bedrock surface, roughness elements, alluvial cover and channels walls. To calculate the contribution of each source, flow resistance has been

weighted by its areal proportion (Tanaka & Izumi, 2013; Inoue et al., 2014; Johnson, 2014; Ferguson et al., 2019). Here we adopted the Johnson (2014) method and assumed the wall flow resistance is negligible, which is valid for a channel that is wide relative to its depth. f can be expressed as a weighted average of the spatial fractions of different sources of flow resistance in the channel

$$f = (1 - F_r - F_a)f_b + F_r f_r + F_a f_a \quad (3)$$

where F_a is the fraction of alluvium, f_b, f_r and f_a are friction factors for bedrock, roughness elements, and alluvium, respectively. Because the deposition of alluvial cover was observed to be negligible in the Fuller Experiments, equation 3 for that case can be simplified to

$$f = (1 - F_r)f_b + F_r f_r. \quad (4)$$

f_b and f_r can be modelled using appropriate roughness length scales in any preferred flow resistance relation. For simplification, they are used here as fitting parameters to calibrate the model to the Fuller Experiments.

Combining equations 1-4 with the continuity equation for a rectangular channel ($Q_w = WhU$), h, U and τ can be solved as

$$h = \left(\frac{Q_w}{W}\right)^{2/3} (8gS)^{-1/3}[(1 - F_r)f_b + F_r f_r]^{1/3} \quad (5)$$

$$U = \left(\frac{Q_w}{W}\right)^{1/3} (8gS)^{1/3}[(1 - F_r)f_b + F_r f_r]^{-1/3} \quad (6)$$

$$\tau = \frac{\rho_w}{8}\left(\frac{Q_w}{W}\right)^{2/3} (8gS)^{2/3}[(1 - F_r)f_b + F_r f_r]^{1/3}. \quad (7)$$

Assuming the roughness elements cause flow separation and contribute form drag, the shear stress available to transport sediment τ_s can be obtained from replacing f in equation 2 with $(1 - F_r)f_b$

$$\tau_s = \frac{\rho_w}{8}\left(\frac{Q_w}{W}\right)^{2/3} (8gS)^{2/3}[(1 - F_r)f_b + F_r f_r]^{-2/3}(1 - F_r)f_b. \quad (8)$$

Initial bedload transport conditions, including the saltation hop height h_s, saltation hop length l_s, bedload particle velocity u_s, are estimated from the empirical relations of Sklar & Dietrich (2004)

$$\frac{l_s}{D} = 8.0(\frac{\tau_s^*}{\tau_c^*} - 1)^{0.88}(1 - (\frac{u^*}{w_f})^2)^{-0.50} \quad (9)$$

$$\frac{h_s}{D} = 1.44(\frac{\tau_s^*}{\tau_c^*} - 1)^{0.56} \quad (10)$$

$$\frac{u_s}{((\frac{\rho_S}{\rho_w} - 1)gD)^{0.5}} = 1.56(\frac{\tau_s^*}{\tau_c^*} - 1)^{0.56} \quad (11)$$

where ρ_s is the sediment density, $u^* = \sqrt{ghS}$ is the flow shear velocity, $\tau_s^* = \tau_s/(\rho_s - \rho_w)\, gD$ is the non-dimensional shear stress available for sediment transport, τ_c^* is τ_s^* at the threshold of motion for particle movement, w_f is the particle fall velocity, which is calculated from the empirical method developed by Dietrich (1982), assuming values of Cory shape factor (0.8) and Powers scale (3.5) typical for natural gravel grains.

The bed-normal velocity w_s is calculated from the difference between the gravitational acceleration of the particle and deceleration due to drag (Lamb et al., 2008)

$$w_s = \sqrt{\frac{C_1}{C_2}(1 - e^{-2C_2(h_s - h_c)})} \quad (12)$$

where $C_1 = (\frac{\rho_s}{\rho_w} - 1)g$ is the gravitational acceleration coefficient, $C_2 = 3C_d D \frac{\rho_w}{\rho_s}$ is the drag deceleration coefficient, C_d (0.45) is the drag coefficient, h_c is the height above the bed of the point of collision with the roughness element ($h_c = 0$ for collisions with the bed).

2.2 Collision between bedload particles and roughness elements

Assuming that the saltating bedload particles have negligible lateral momentum during the normal course of a downstream hop, the saltation lateral velocity v_s before collision is zero. Thus, the incoming saltation velocity vector $\boldsymbol{i_s}$ has two non-zero components

$$\boldsymbol{i_s} = (u_s, 0, w_s). \quad (13)$$

During collision with roughness elements in water, bedload particles experience an inelastic rebound that can be modelled by the sum of an elastic and a viscous force (Cundall & Strack, 1979). For simplicity, the elastic response is modelled using a reflection methodology to calculate the outgoing saltation velocity vector after collision with a roughness element as

$$\boldsymbol{o_s} = C_r(\boldsymbol{i_s} - \boldsymbol{2p}) \quad (14)$$

where $\boldsymbol{p}$ is the projection of the incoming particle velocity vector onto the surface normal vector, at the point of collision (defined by the normal vector $\hat{\boldsymbol{n}}$) calculated from

$$\boldsymbol{p} = (\frac{\boldsymbol{i_s} \cdot \hat{\boldsymbol{n}}}{\hat{\boldsymbol{n}} \cdot \hat{\boldsymbol{n}}})\hat{\boldsymbol{n}} \quad (15)$$

assuming that the tangential force during collision is negligible. The coefficient of restitution (C_r) describes the retention of particle momentum during the collision between bedload particles and roughness elements. We choose a value $C_r = 0.9$, which means that the particle loses $1 - C_r^2 = 19\%$ of its incident kinetic energy during an impact. Although this value of C_r is above the theoretical prediction of Davis et al. (1986) for elastic spheres ($C_r = 0.65$), it is within the range of experimental observations (Niño et al., 1994; Schmeeckle et al., 2001; Joseph et al., 2001; Joseph & Hunt, 2004) for gravel spheres at high Stokes number.

The magnitude and direction of $\boldsymbol{o_s} = (u_o, v_o, w_0)$ are controlled by $\boldsymbol{i_s}$ and $\hat{\boldsymbol{n}}$ at the point of collision (Figure 3). Consider a bedload particle that collides near the base of the roughness element, at the roughness element centerline. The magnitude of $\boldsymbol{i_s}$ for this case is maximized because the collision occurs near the bed where w_s is the greatest, which will maximize the magnitude of $\boldsymbol{o_s}$ for given hydraulic conditions. However, the collision will create an $\boldsymbol{o_s}$ for this case that points in the upstream direction with negligible lateral velocity v_o, because $\hat{\boldsymbol{n}}$ is pointing upstream (Figure 3). In contrast, $\boldsymbol{o_s}$ will have a substantial wall-normal velocity component v_o with negligible downstream velocity component u_0 when $\hat{\boldsymbol{n}}$ is rotated to 45 degrees relative to the centerline of the roughness element (Figure 3). Therefore, to incorporate the variation of $\boldsymbol{i_s}$, $\hat{\boldsymbol{n}}$ and hence $\boldsymbol{o_s}$ at the point of collision with the roughness element, the surface of each roughness element is discretized into N approximately uniform triangular grid cells ($N \approx 2000$ is selected here for a balance of efficiency and accuracy).

Within each cell, the potential impact position and impact angle are assumed to be represented the cell centroid, and the outgoing velocity $\boldsymbol{o_s}$ of individual bedload particles is calculated in each grid cell from equations 13-15.

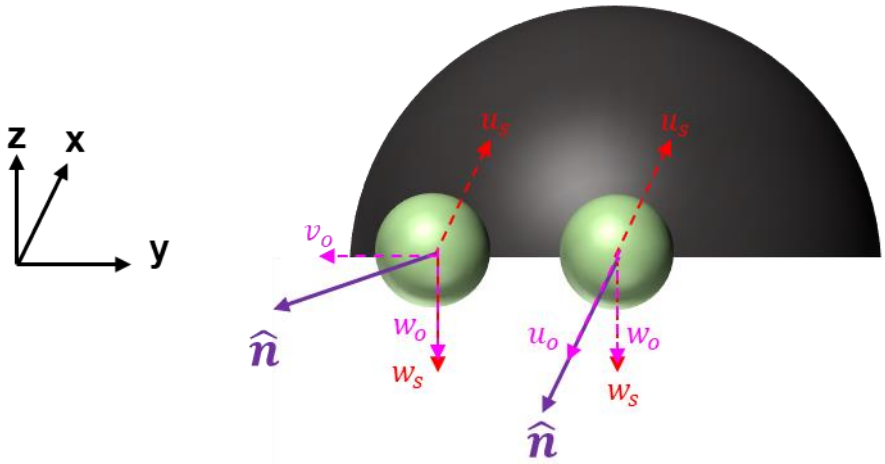

Figure 3 Schematic diagram of collision between roughness element (black) and bedload particles (green). The incoming velocity $\boldsymbol{i_s} = (u_s, 0, w_s)$, where u_s is incoming downstream velocity and w_s is incoming vertical velocity. The outgoing velocity $\boldsymbol{o_s} = (u_o, v_o, w_o)$, where u_0 is outgoing downstream velocity, v_0 is outgoing lateral velocity and w_0 is outgoing vertical velocity. Two examples of collision are shown here: collision with the roughness element head resulting in $v_o \approx 0$ and collision with 45 degrees relative to the base of the roughness element head resulting in $v_o \gg 0$.

Not all cells on the surface of a semi-spherical roughness element are subject to collisions. To estimate which cells will experience collisions, and the impact rate on each grid cell as a function of the bedload flux, we begin by assuming that the trajectory of bedload particles before impacting on the roughness element is composed of two components: upward trajectory and downward trajectory (Sklar & Dietrich, 2004). The upward trajectory has a hop height of h_s and a hop length of l_{su}, and the downward trajectory has a hop height of h_s and a hop length of l_{sd}. Assuming these two trajectories together form a triangle, with a total hop length of l_s and hop height of h_s (Figure 4), l_{su} and l_{sd} can be approximated from l_s as (Sklar & Dietrich, 2004)

$$l_{su} = \frac{1}{3} l_s \tag{16}$$

$$l_{sd} = \frac{2}{3} l_s \tag{17}.$$

Three planes are formed by the triangular trajectory of bedload particles: 1) the plane parallel to the upward trajectory; 2) the plane parallel to the downward trajectory; and 3) the plane parallel to the bed (Figure 4). All upward moving particles must move parallel to the first plane and all downward moving particles must cross the first plane. In contrast, only upward moving particles will cross the second plane and all downward moving particles will follow the second plane. The third plane, the channel bed, is where the particles turn around. Our

model only incorporates the impacts of downward moving particles on the roughness element surface. The length L of the first plane for intercepting the downward moving particles is

$$L = \sqrt{h_s^2 + l_{su}^2} \tag{18}$$

and its angle α intersecting with the bed is

$$\alpha = \arctan\frac{h_s}{l_{su}} \tag{19}$$

The impact rate, with dimensions of collisions per unit time per unit area on the first plane, can be expressed as

$$I_p = \frac{q_s}{ML} \tag{20}$$

where q_s is sediment supply per unit width, and M is the mass of a bedload particle. The area of each grid cell is projected onto the first plane, along a vector parallel to the downward trajectory of bedload particles, to calculate the impact rate on each grid cell. The angle β of the projected direction intersecting with the bed is (Figure 4)

$$\beta = \arctan\frac{h_s}{l_{sd}} \tag{21}.$$

The projected area for each grid cell is defined as A_c. The impact rate on each grid cell of the roughness element surface I_c can hence be expressed as

$$I_c = I_p A_c \tag{22}$$

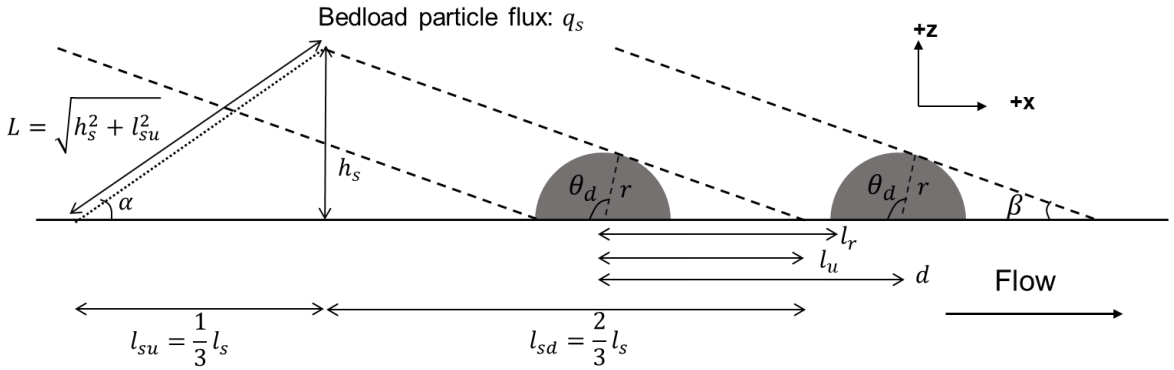

Figure 4 Sketch of calculating the impact rate on the roughness element (grey semi-circle). The trajectory for bedload particle flux is simplified as a triangle, formed by upward l_{su} and downward portion l_{sd} of the total hop length l_s and total hop height h_s. Three planes are defined here, including the plane parallel to the upward trajectory (dotted line) intersected with the bed from an angle α, the plane parallel to the downward trajectory (dashed line) intersected with the bed from an angle β, and the plane of the bed where the particles turn around (solid line). Each plane is as wide as the channel.

Limits also exist on impact positions on both the downstream and upstream facing parts of the roughness elements. Bedload particles moving downstream cannot impact the downstream face of the roughness element below the tangent point (Figure 4) which has a central angle θ_d calculated from

$$\theta_d = \frac{\pi}{2} + \beta \ . \tag{23}$$

Whether a particle impacts the upstream facing part of the roughness element is controlled by the relation between the downstream distance of the potential impact position on the bed l_u and the distance between the center of the roughness element and the vertex of the upstream face of the successive downstream roughness element l_r (Figure 4)

$$l_u = \frac{r}{\sin\beta} \tag{24}$$

$$l_r = d - r \tag{25}$$

where r is the semi-circle radius cut along the roughness element in the downstream direction, which decreases from center line of the roughness element laterally. When l_u is equal or smaller than l_r ($l_u \leq l_r$), the downstream trajectory of bedload particles at the tangent line can impact on the bed directly (Figure 4). Therefore, the bedload particles can impact any positions on the upstream facing part of the roughness element. However, if $l_u > l_r$, the downstream trajectory of bedload particles at the tangent line is intercepted by the upstream facing part of the subsequent downstream roughness element instead of impacting on the bed.

The limitation and variation of impact rates I_c are illustrated in Figure 5, where the 4.3 mm and 10 mm roughness elements from the Fuller Experiments are used as examples. The center of each grid cell is projected onto a horizontal 2D surface. There is no impact on most of the downstream facing part of the semi-sphere surface that is below the tangent point of downward moving trajectory (Figure 5). Meanwhile, the impact rate is zero near the vertex of the upstream facing part of the roughness element (Figure 5), because the impacts here are in the shadow of downward moving trajectory when $l_u > l_r$. The impacts decrease from the center to the edge of the roughness element (Figure 5), due to the decrease of the shadow effect as the radius r of a circle for a longitudinal slice through the sphere reduces to zero at the edge of the roughness. The impact rate also decreases with distance downstream because the impact area A_c goes to zero when the surface cell gets tangential (parallel) to the flux trajectory (Figure 5).

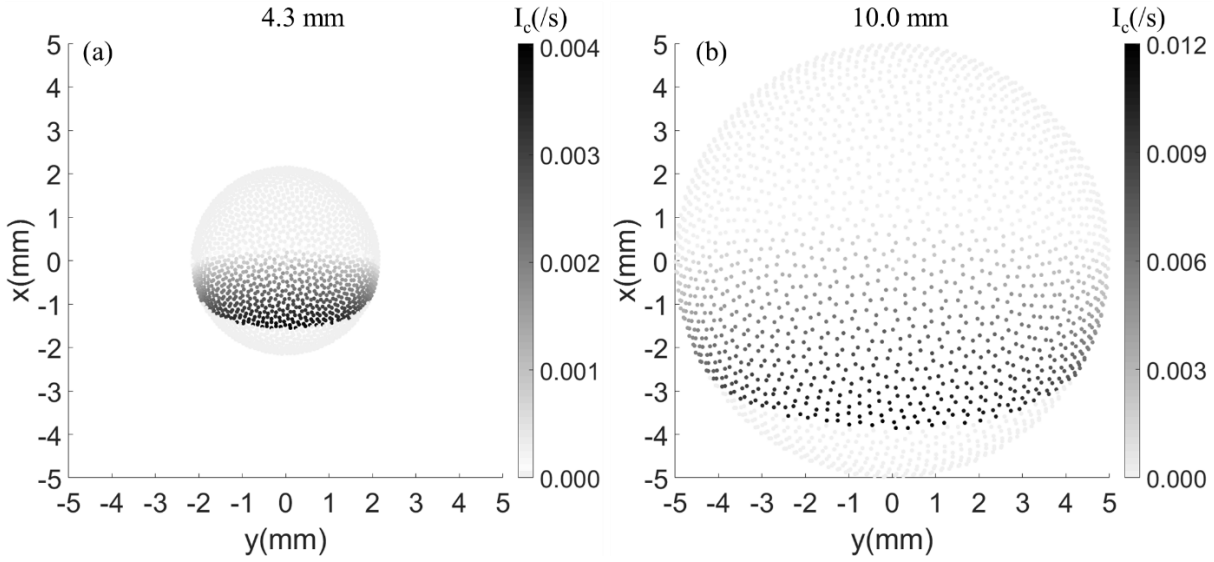

Figure 5 Distribution of impact rates on each grid cell of roughness elements with diameter of a) 4.3 mm and b) 10.0 mm using models inputs from the Fuller Experiments.

2.3 Movement of bedload particles from collision with roughness element to impact on the wall

After collision, the movement of bedload particles is modelled from force balance equations and tracked over each time step Δt. We assume that fluid drag and gravity are the dominant forces affecting instantaneous downstream velocity u, lateral velocity v and vertical velocity w. The change in particle velocities with time are given by

$$-\frac{du}{dt} = C_2(u - U_z)^2 \tag{26}$$

$$-\frac{dv}{dt} = C_2 v^2 \tag{27}$$

$$-\frac{dw}{dt} = \begin{cases} C_2 w^2 + C_1 & for\ w > 0 \\ C_2 w^2 - C_1 & for\ w \leq 0 \end{cases} \tag{28}$$

where U_z is the downstream flow velocity at height z above the bed. For turbulent boundary layer flow in a channel, U_z can be calculated from the law of the wall

$$U_z = \frac{u^*}{\kappa}\ln(\frac{30z}{k_s}) \tag{29}$$

where κ is von Karman's constant (~ 0.41), k_s is the hydraulic roughness length scale which can be obtained from friction factor f using a general Manning-Strickler formula

$$k_s = h(8f)^3 \tag{30}$$

(Johnson, 2014). Equations 26-28 can be numerically integrated at each time step Δt to solve for the velocity and position of individual bedload particles. The time step used in the simulation is $\Delta t = 10^{-5}$s. Smaller time steps were also tested, which substantially increase the computational time but do not change the results. A minimum wall-normal velocity v_{min} is adopted here to distinguish between impacts that cause erosion and impacts that are viscously damped, which is a function of the particle Stokes number S_t (Davis et al., 1986; Schmeeckle et al., 2001; Joseph & Hunt, 2004):

$$v_{min} = \frac{9S_t\rho_w\nu}{\rho_s D} \tag{31}$$

where ν is the kinematic viscosity of the fluid (10^{-6} m^{2}s^{-1}), and a value of $S_t = 100$ is selected here from Schmeeckle et al. (2001) and Joseph & Hunt (2004). At each time step, a bedload particle may be rebounded by the channel bed or other roughness elements before it impacts on the wall (Figure 6). In this situation, the rebounded velocity is simulated using the same method used for the original collision with the roughness element, taking into account that the normal vector for the bed is vertical. The simulation runs until a bedload particle has impacted the wall or its lateral velocity is below the velocity limit v_{min} before reaching the wall. When bedload particles impact the wall, the impact velocity vector $\boldsymbol{IV} = (u_i, v_i, w_i)$ and impact position vector $\boldsymbol{IL} = (x_l, y_l, z_l)$ are recorded for calculation of lateral erosion rate of different locations on the wall.

The deflection trajectories of bedload particles vary with the impact positions on the same roughness element. Bedload particles impacting on the part that is near 45 degrees relative to the centerline of roughness element travel a shorter downstream distance because the particles have larger lateral velocity and can impact on the wall faster (Figure 6a). Meanwhile, bedload particles deflected by the higher part of the roughness element can impact higher on the wall due to the higher initial height before deflection and the upward moving velocity after deflection here (Figure 6b). When the roughness elements are located further from the wall, more impacts are viscously damped and are rebounded by the bed before impacting on the wall due to more loss of momentum on the way to the wall (Figure 6). The bedload particles deflected by the roughness elements further from the wall also impact lower on the wall (Figure 6a), and impact further downstream on the wall as it takes longer to impact on the wall (Figure 6b).

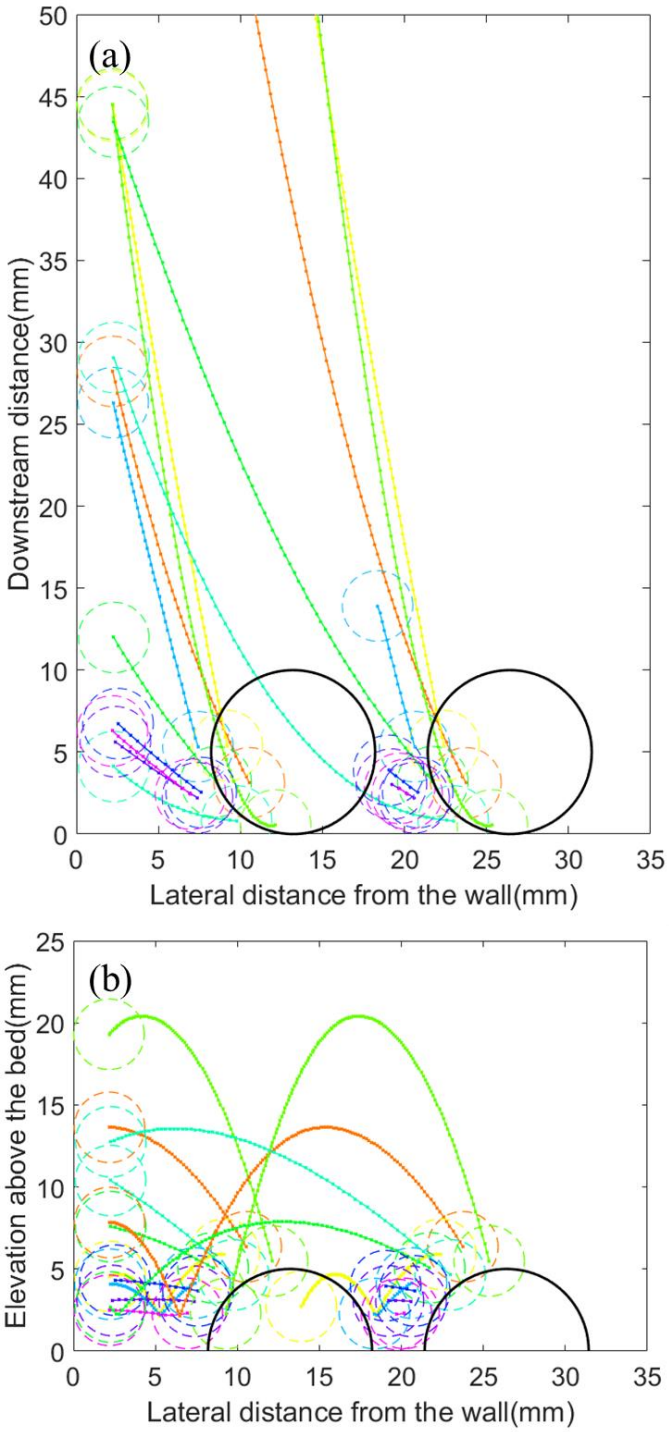

Figure 6 a) Plan view and b) downstream view of the deflection trajectories of bedload particles (colorful circles with dashed lines) for a range of deflection positions on the roughness elements (black circles and semi-circles with solid lines). The roughness size is 10.0 mm and the bedload particle size is 4.3 mm. The model inputs are from the Fuller Experiments.

411 *2.4 Calculation of instantaneous lateral erosion rate*

412 Assuming the channel wall is fully exposed to impacts, the erosion rate E_c due to deflections
413 from one grid cell on a roughness element, can be expressed as the product of two terms: the
414 volume eroded per particle impact V_c and the number of particle impacts per unit time I_w
415 (Sklar & Dietrich, 2004)

416 $$E_c = V_c I_w \tag{32}$$

417 where V_c can be calculated as a function of impact velocity v_i, and rock parameters, including
418 Young's modulus of elasticity of the bedrock Y, dimensionless bedrock strength coefficient
419 k_v, and tensile yield strength σ_T

420 $$V_c = \frac{\pi \rho_s D^3 v_i^2 Y}{6 k_v \sigma_T^2}\,. \tag{33}$$

421 I_w can be determined from I_c depending on whether the movement of bedload particle
422 deflected by each cell will lead to an impact on the wall or not. If the bedload particle
423 deflected by the roughness element does not impact on the wall, its impact rate on the wall I_w
424 is zero. However, if the bedload particle obtains enough momentum to reach the wall, its
425 impact rate on the wall I_w is the same with that on the roughness element I_c.

426 $$I_w = \begin{cases} I_c & impacts\ on\ the\ wall \\ 0 & not\ impacts\ on\ the\ wall \end{cases} \tag{34}$$

427 E_c varies with each grid cell on a roughness element (Figure 7). Only the 1/4 of the semi-
428 sphere roughness element that faces upstream and toward the near wall contributes to E_c due
429 to the concentration of impacts on the upstream facing part of the semi-sphere (Figure 5) and
430 the deflection of bedload particles towards the other side of the channel if they impact on the
431 roughness element surface that faces against the wall (Figure 7). E_c is highest at the impact
432 position that has a normal vector $\widehat{\boldsymbol{n}}$ facing 45 degrees relative to the longitudinal centerline of
433 the roughness element in planview, and is close to the base of the roughness element, because
434 the rebounded velocity (Figure 3) and the impact rate (Figure 5) are highest there. E_c
435 decreases with the increasing distance between the roughness element and the wall due to the
436 loss of lateral momentum of bedload particles when travelling towards the wall (Figure 7).

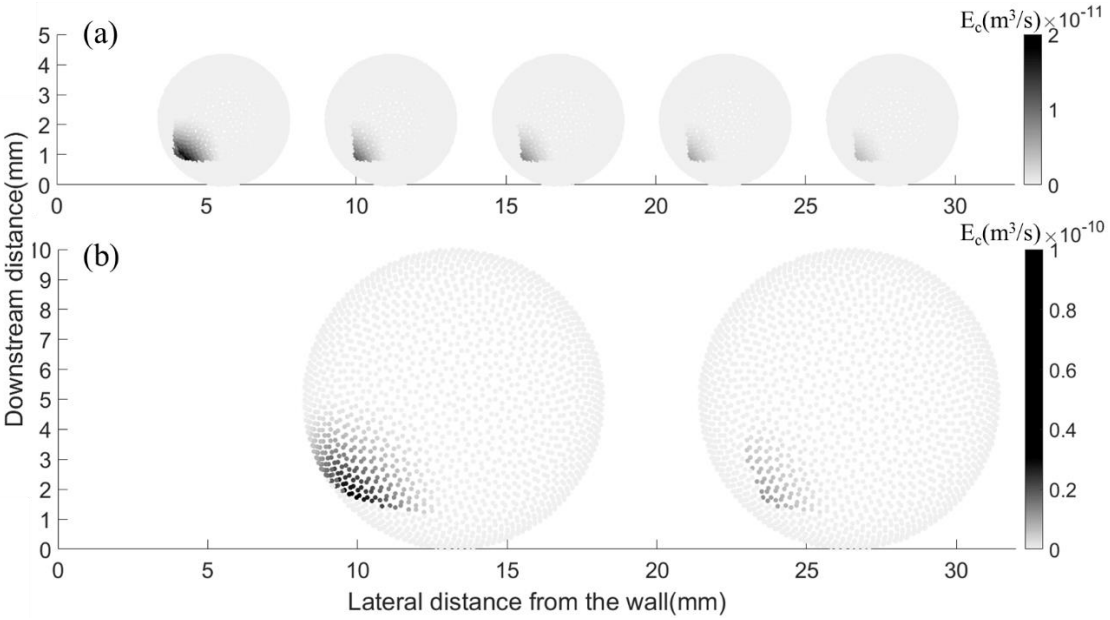

Figure 7 Variation of E_c with each grid cell on the a) 4.3 mm roughness elements and b) 10.0 mm roughness elements using inputs from the Fuller Experiments.

Assuming that bed roughness elements are uniformly distributed in rows comprised of equally spaced semi-spheres (Figure 2), and transported bedload is uniformly distributed across the channel, each row of roughness elements deflects same number of bedload particles and causes same amount of lateral wall erosion. Therefore, only one row of roughness elements is used for calculating the instantaneous local lateral erosion rate E_c and the total erosion rate E_t due to the existence of one row of roughness elements is simply the sum of all E_c, the local erosion rates due to individual bedload particles deflected by each grid cell on the roughness elements

$$E_t = \sum E_c \tag{35}$$

Because the total erosion rate due to multiple rows of roughness elements is the superposition of the lateral erosion rate due to a single row of roughness elements, and the lateral erosion rate in the longitudinal direction repeats for the downstream distance d between two adjacent rows of roughness elements, the integrated lateral erosion rate within d due to multiple rows of roughness element is equal to E_t. Therefore, the averaged area of material removed from the channel cross section per unit time (referred to as bulk erosion rate E_b) within d can be expressed as

$$E_b = \frac{E_t}{d} \tag{36}$$

Bedload particles impact on the wall at many different elevations and downstream locations (Figure 6). To calculate the average lateral erosion rate E_z at a given elevation z, the wall is divided into a uniform grid with a vertical interval Δz from the base of the wall to the maximum erosion height on the wall z_{lmax}. A value of $\Delta z = 1$ mm is selected here in accordance with the experimental results of Fuller et al. (2016); and z_{lmax} is obtained from the distribution of the height z_l of all impacts.

The impact area within each grid A_w is

$$A_w = d\Delta z \tag{37}$$

The lateral erosion rate E_z for a given elevation range $z + \Delta z$ can be calculated as a sum of the volume eroded by impacts that fall within that elevation range divided by the impact area A_w

$$E_z = \frac{\sum_{z_l \in z} E_c(z_l)}{A_w} \tag{38}.$$

2.5 Co-evolution of lateral erosion rate, wall morphology and shear stress

As the wall is eroded over time, the travel distance, and hence the potential for loss of momentum of bedload particles after collision with the roughness element, will increase, resulting in lower instantaneous lateral erosion rates. Meanwhile, the cross-sectional area of the flow will change as the wall is eroded, becoming wider and shallower. This results in a somewhat lower bed shear stress and hence lower lateral erosion rate. In turn, the lower lateral erosion rate will slow down the wall evolution. Without considering the co-evolution between shear stress and lateral erosion rate, the model will exaggerate wall evolution.

To model the effects of wall evolution, we break the simulation into a sequence of time periods, each time period T lasting 10 minutes. Smaller time periods were tested, but did not influence the results. During each period we assume that the flow depth, and thus shear stress, do not change. We average the erosion rate from impacts that occur during that time period. Then for the next period we update the depth and shear stress, and calculate new erosion rates. At beginning of the simulation ($T = 1$), the initial depth and shear stress are obtained from assuming a rectangular cross section from equations 1-8. As the wall is eroded over time, the channel cross section and hence the wetted area become irregular. Therefore, $Q_w(T)$ is not simply a product of $W(T)$, $h(T)$, and $U(T)$ at the time period $T > 1$. Instead, $Q_w(T)$ needs to calculated from the wetted area $A(T)$ over the irregular cross section of the flow

$$Q_w(T) = A(T)U(T) \tag{39}$$

where $A(T)$ is a function of flow depth $h(T)$ and needs to be obtained from integrating the flow width over $h(T)$ for a given cross section shape. We assume that the friction factor f is constant over the run period, because the changes of flow depth are relatively small. Combining equation 39 with equations 1-6, $h(T)$ can be expressed as

$$h(T) = \frac{1}{8gS}\left(\frac{Q_w}{A(T)}\right)^2 [(1 - F_r)f_b + F_r f_r] \tag{40}$$

$h(T)$ and $A(T)$ can be solved from equation 40 by starting with an initial guess of $h(T)$, integrating the flow width over $h(T)$ for the current cross section shape to get $A(T)$ and iteratively changing the values of $h(T)$ and $A(T)$ until these two solutions converge in equation 40. $U(T)$ will then be back-calculated from equation 39, and used to get the total shear stress $\tau(T)$ and shear stress available for sediment transport $\tau_s(T)$ from total friction factor $f = (1 - F_r)f_b + F_r f_r$ and bedrock friction factor $(1 - F_r)f_b$ using equation 2, respectively

$$\tau(T) = \frac{\rho_w[(1-F_r)f_b + F_r f_r]U(T)^2}{8} \tag{41}$$

$$\tau_s(T) = \frac{\rho_w(1-F_r)f_b U(T)^2}{8}. \quad (42)$$

4. Results

We assessed model performance using results from laboratory experiments reported by Fuller et al. (2016). Fuller et al. (2016) constructed three experimental channels (referred to as channels C1, C2 and C3), held the water discharge and sediment supply constant for each channel throughout the experiment, but varied the roughness element size over six classes: no roughness elements (smooth sections); 2.4 mm; 4.3 mm; 7.0 mm; 10.0 mm; and 16.0 mm (roughness sections). Table 1 and Table 2 list the initial hydraulic and sediment transport conditions in the Fuller Experiments, and the values of parameters used in the model calculations. These experiments provide an ideal test case for our model because the flow depth and thus initial shear stress available for sediment transport was measured, and erosion rates and patterns are measured for the various roughness element sizes. However, the rock tensile strength σ_T which controls the magnitude of the erosion rate was not measured. For the model calculations we use a value of 5.5×10^4 Pa for σ_T, which is calibrated from the bulk erosion rate of 10 mm roughness elements ($E_b = 74$ mm^2/hr) in Channel C3. This value is reasonable for the weak concrete used in the Fuller Experiments (Sklar & Dietrich, 2001), and is used for predicting the erosion rate and assessing the model performance for other roughness element sizes.

Table 1 Initial hydraulic and bedload transport conditions used in the simulation of the Fuller Experiments

Channel section	D_r[b] (mm)	F_r[b]	d[c] (mm)	W[b](1[a]) (mm)	Q_w[b] (×10^{-3}m^3/s)	q_s[b] (kg/m/s)	τ[b](1[a]) (Pa)	τ_g[b](1[a]) (Pa)	f_r[d]	f_b[d]
C2	2.4	0.34	3.65	183	12.9	0.21	18.6	14.9	0.10	0.21
C3	4.3	0.47	5.58	165	12.9	0.19	14	13	0.0091	0.10
C1	7.0	0.50	8.75	160	12.7	0.19	12	11.6	0.0024	0.070
C2[e]	10.0	0.51	13.2	181	12.9	0.21	18.3	9.2	0.16	0.16
C2	16.0	0.56	19.5	183	12.9	0.21	26.4	8	0.61	0.34

[a] 1 indicates the initial conditions, prior to wall evolution.
[b] directly from Fuller et al. (2016).
[c] calculated from F_r by Fuller et al. (2016) assuming the roughness elements are uniformly distributed.
[d] calibrated from τ and τ_s by Fuller et al. (2016).
[e] 10.0 mm roughness elements are located both in C2 and C3 by Fuller et al. (2016), the one in C3 is used for calibration of σ_T and the one in C2 is used for model performance.

Table 2 Parameters used in simulation of the Fuller Experiments

Variable	Value
Bedload particle size D (mm)	4.3 [a]
Channel slope S	0.025 [a]
Critical Shields stress τ_c^*	0.045 [b]
Water density ρ_w (kg/m^3)	1000 [b]
Sediment density ρ_s (kg/m^3)	2650 [b]
Rock elastic modulus Y (Pa)	5×10^{10} [c]
Restitution coefficient C_r	0.9 [b]
Dimensionless rock resistance parameter k_v	10^6 [c]
Rock tensile strength σ_T (Pa)	5.5×10^4 [d]
Time period ΔT (min)	10 [b]
Time step Δt (s)	10^{-5} [b]

[a] From Fuller et al. (2016).
[b] Assumed.
[c] From Sklar and Dietrich (2004).
[d] From calibration with the 10 mm roughness element in C3 by Fuller et al. (2016).

4.1 Model performance

We assessed three aspects of the model performance when comparing to the Fuller Experiments: 1) shape of the eroded profile, 2) peak erosion rate, and 3) bulk (integrated) cross-section erosion rate. Figure 8 shows the erosion rates measured in the Fuller Experiments. An undercut wall morphology occurred, with erosion below ~ 25 mm on the wall for all roughness sections. Lateral erosion was concentrated in the lower half of the undercut (5 mm - 10 mm) and decreased progressively up to the maximum height of erosion. The peak erosion rate was similar for each roughness section, occurring between a height of 5 mm and 10 mm over 2.15 hr.

The model without co-evolving the shear stress, wall morphology and erosion rate captures the concentration of erosion in the lower half of the wall observed in the Fuller Experiments (Figure 8). However, it overpredicts the peak erosion rate by 3 to 5 times, except the 2.4 mm roughness element where the measured peak erosion rate is slightly larger (~ 10%). The elevation of the peak erosion rate concentrates in a smaller zone near the bottom of the wall (below 5 mm), while the Fuller Experiments show a wider zone of peak erosion rate spreading from the base of the wall to the middle of the erosion zone (below 10 mm). The erosion rate below the radius of bedload particles is under-predicted by the model compared with the substantial undercut on the wall observed in the Fuller Experiments (Figure 8) due to the assumption of spherical bedload particles, which cannot impact on the wall below their radius.

To allow a normalized comparison of bulk erosion rate between model predictions and the Fuller Experiments solely because of the occurrence of roughness, we follow the method by Fuller et al. (2016) in their Figure 9 and subtracted the bulk erosion rate measured in the smooth section of the same channel from the bulk erosion rate in sections with roughness elements. The Fuller Experiments produced a roughly parabolic relation between the roughness element size and integrated cross-section erosion (Figure 9), which increases with roughness size below 4.3 mm, peaks at 4.3 mm, and then gradually decreases with larger roughness element sizes. Although the model captures this parabolic relation observed in the Fuller Experiments, it overpredicts the erosion for all roughness sections by 1.2 to 2 times.

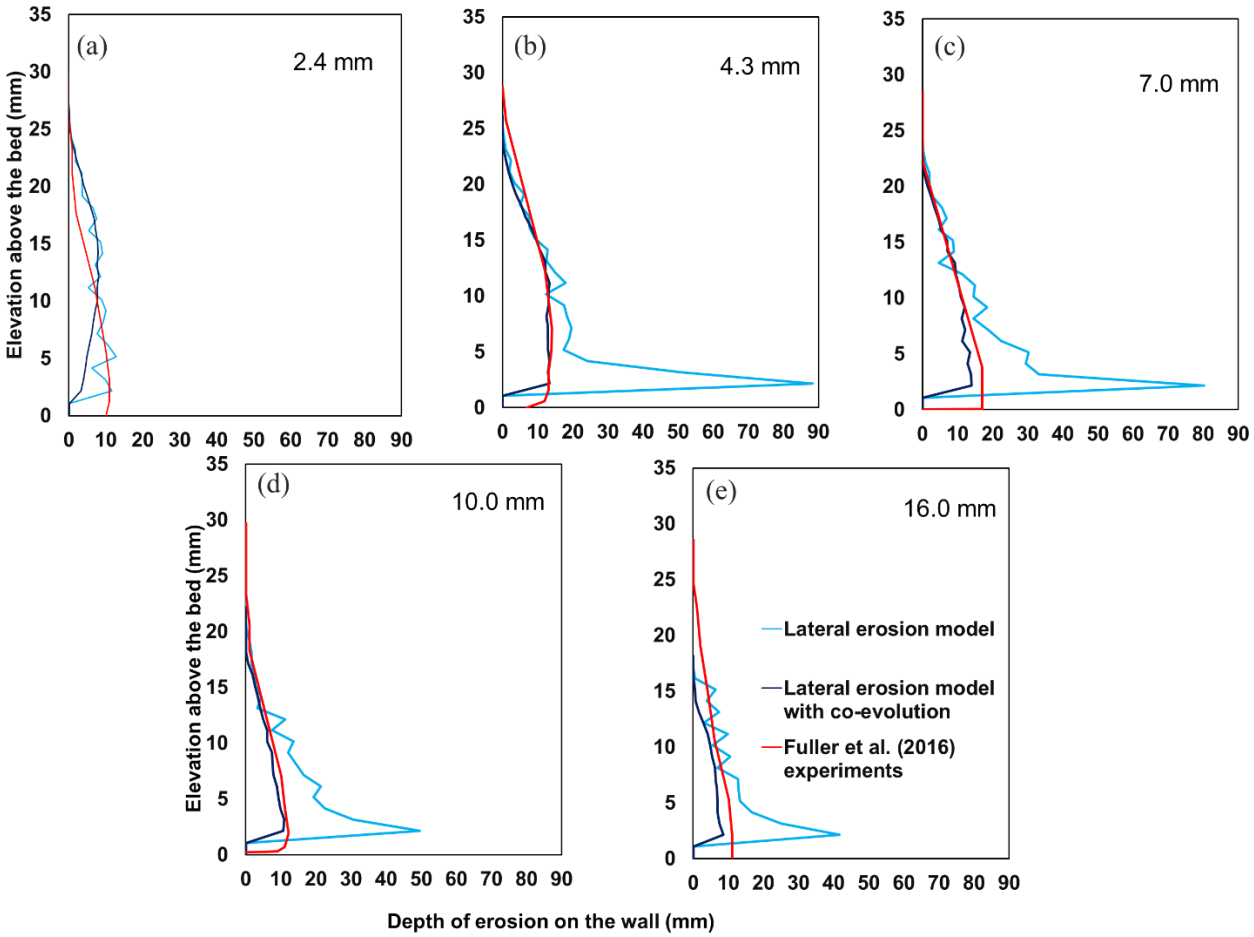

Figure 8 Comparison of modelled cross section shape and peak erosion rate to the Fuller Experiments for a) 2.4 mm, b) 4.3 mm, c) 7.0 mm, d) 10.0 mm and e) 16.0 mm roughness sections.

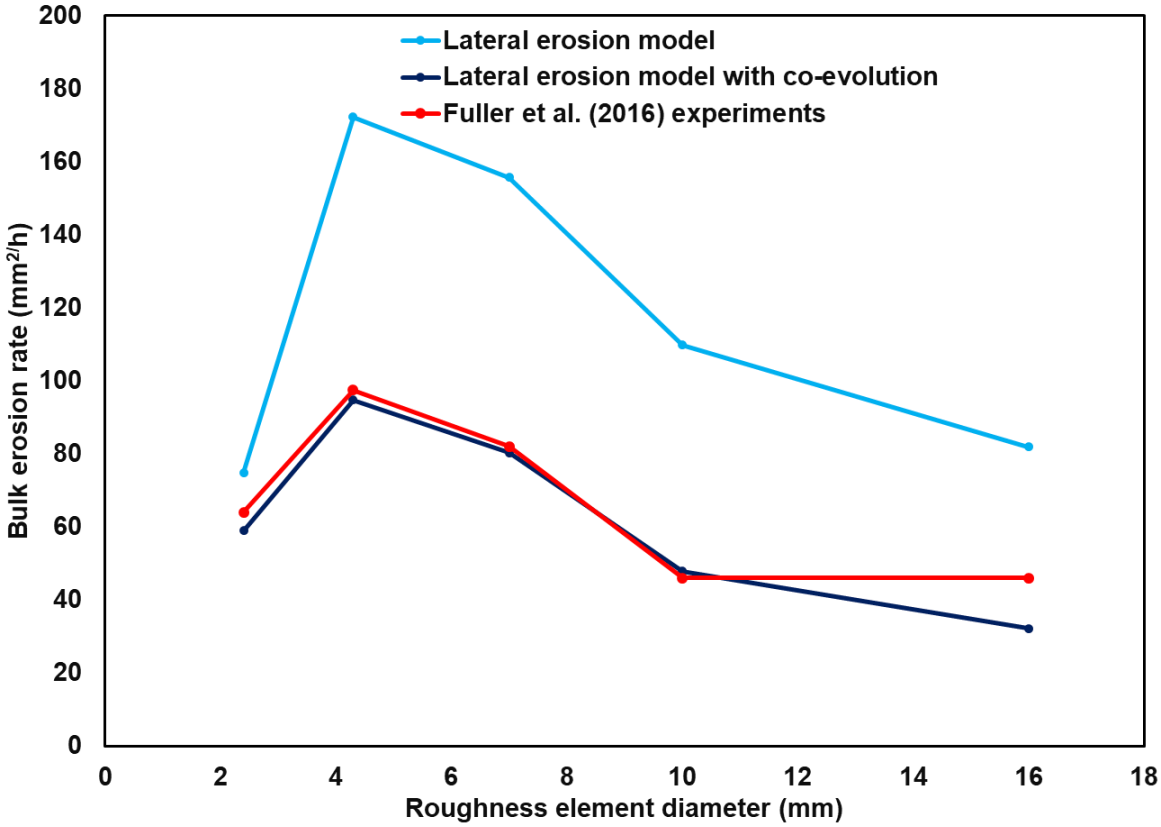

Figure 9 Comparison of the total (integrated) cross-section erosion between model predictions and the Fuller Experiments for 2.4 mm, 4.3 mm, 7.0 mm, 10.0 mm in Channel 3 (C3), 10.0 mm in Channel 2 (C2) and 16.0 mm roughness sections.

The deviation in the erosion profile and peak erosion rate between the model predictions and the Fuller Experiments can occur because changes in wall morphology will cause a decline in shear stress applied to the bed. As the wall is eroded over time, the shear stress will drop and the travel distance for individual particles will increase, resulting in a lower erosion rate over time. We explored the hypothesis that shear stress needs to co-evolve with morphology to accurately predict erosion rate by dividing the model run into 10 minute periods. For each period, we calculated the suite of particle deflections and resulting erosion rates, then updated the wall morphology, used it recalculate the water depth, water velocity and shear stress available for sediment transport in the next time period from equations 39-42), and updated the particle impact velocity, particle impact rates and erosion rates at next period. The initial model inputs are from measurements by the Fuller Experiments (Table 1 and 2), and each model run is 2.15 hr.

Figure 10 shows the decline in mean velocity and shear stress that occurs due to the increase in cross-sectional area as the wall is undercut. The change in cross-sectional area, velocity, and shear stress is subtle. Shear stress declines most over the first time period (10 min) but barely changes for the rest of the time, because the erosion rate is largest in that first time period, when the bedload particle travel distance is smallest. The overall decline in shear stress is ~10%, because the changes in wall morphology are relatively small. Only the bottom of the wall is eroded and the maximum eroded length is only ~ 10% of the total river width. Our assumption of constant friction factor f may also slow down the change of shear stress.

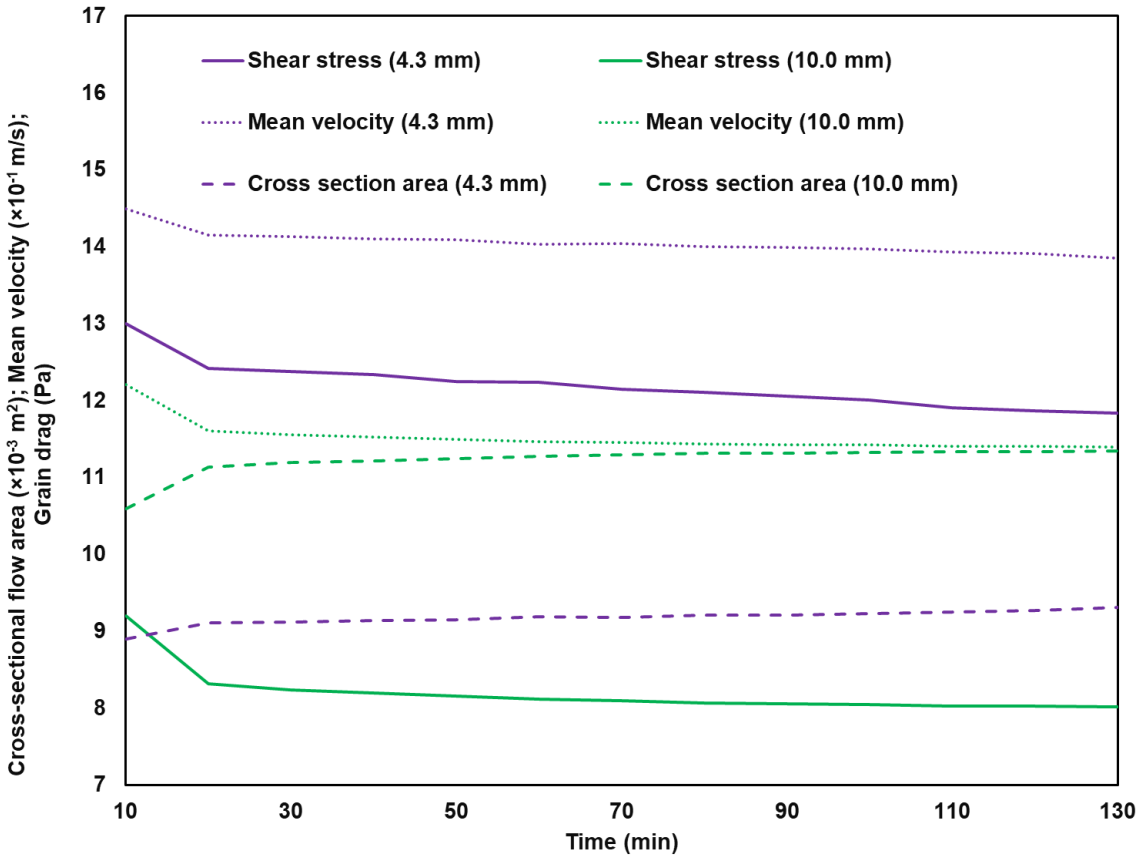

Figure 10 Cross section area of flow, mean velocity and shear stress evolution for 4.3 mm and 10.0 mm roughness element

The model, when coupled with wall evolution, produces an undercut wall shape that matches the Fuller Experiments well (Figure 8). The simulated erosion concentrates in the lower half of the erosion zone and tapers off with increasing height on the walls. The predicted peak erosion depth on the wall generally ranges from 8 mm to 15 mm for all roughness sections, as in the experiments. However, the peak erosion is slightly less than that in the experiments, by ~ 2 mm over the total time period. We suspect this is because we neglected the influence of turbulence on lateral bedload particle deflection into the wall. The Fuller Experiments with a planar bed and no deflectors had a wall erosion depth of ~2 mm over the 2.15 hr run duration (See Figure 6d by Fuller et al., 2016). The model with evolution of the wall and shear stress also successfully reproduces the parabolic relation between the roughness element size and integrated cross-section erosion, and the magnitude of erosion over all roughness sections.

The model is suitable for predicting the instantaneous lateral erosion rate on the wall. To successfully predict the change of wall morphology over time, however, the model needs to be coupled with co-evolution of shear stress, wall morphology and lateral erosion rate.

4.2 Evolution of instantaneous lateral erosion rate and wall morphology

The modelled evolution of erosion rate and wall morphology is similar for all channels in the Fuller Experiments. Representative profiles, for the 4.3 and 10 mm roughness elements, of lateral erosion rate and wall morphology evolution through time are shown in Figure 11 and Figure 12, respectively. The instantaneous erosion rate declines over time (Figure 11). Erosion rate is roughly 10 times lower in the final time period compared to the initial time

period. As the wall is eroded over time, the shear stress declines with the mean flow velocity (Figure 9), which leads to a lower erosion rate by decreasing the impact velocity on the wall in later time periods. However, the shear stress at the end of the time period is ~ 90 % of the initial shear stress (Figure 9), indicating the influence of the decreasing shear stress on erosion rate is almost negligible over the time period here. The decreasing erosion rate over time is largely due to the longer travel distance from deflection on the roughness element to impact on the wall as the wall is eroded over time (Figure 12). The erosion rates do not decline to zero over the 2.15 hr model runs, but the rate of wall evolution does decline (Figure 12).

The erosion rate decreases in the lower half of the erosion zone, but barely changes in the upper half. At the beginning of the time period, the erosion rate is roughly 10 times smaller in the upper half of the erosion zone, compared to its lower half (Figure 11). At the end of the time period, the erosion rate in the upper and lower halves of the erosion zone are similar. The combined effect of this vertical variation through time is a uniform erosion pattern on the wall over the 2.15 hr simulation time (Figure 12).

The elevation of the peak erosion rate on the wall gets higher from ~2.5 mm to ~8 mm above the bed (Figure 11). Initially, the maximum erosion rate is mostly created by impacts of downward moving bedload particles, which concentrates in a zone near the base of the wall. As the wall is eroded over time, however, the corner between the bed and the wall is protected as it has been undercut. Instead, more bedload particles will either impact higher on the wall or impact on the bed, obtain upward momentum and bounce up on the wall. The elevated position of the peak erosion rate on the wall elevates the concentration of erosion zone on the wall (Figure 12).

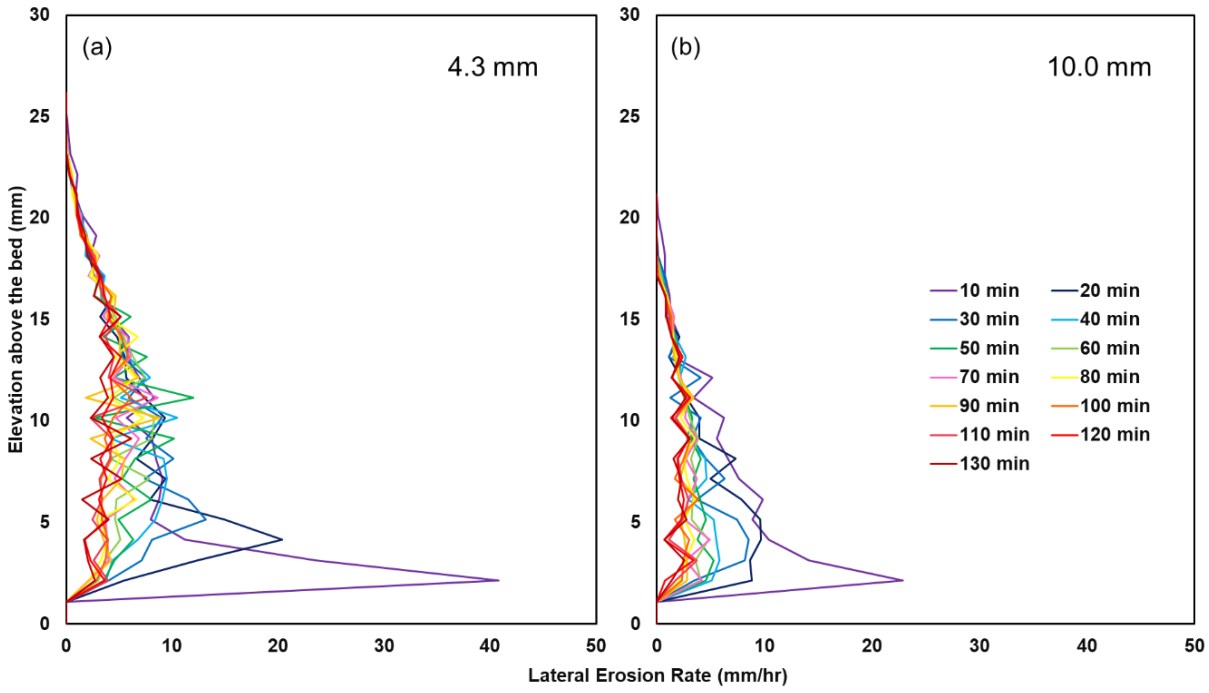

Figure 11 Evolution of instantaneous lateral erosion rate on the wall for a) 4.3 mm and b) 10.0 mm roughness sections over 2.15 hr

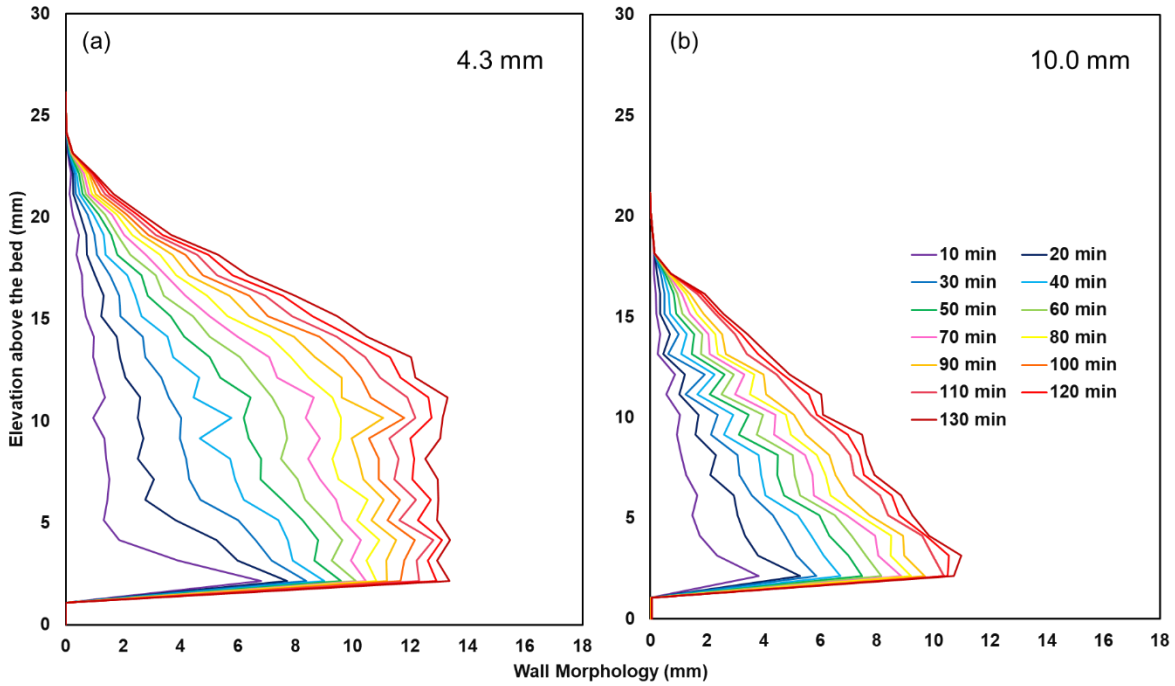

Figure 12 Evolution of wall morphology for a) 4.3 mm and b) 10.0 mm roughness sections over 2.15 hr

5. Coupled lateral and vertical erosion model

Both field observations (Hartshorn et al., 2002; Turowski et al., 2008b; Fuller et al., 2009; Finnegan & Balco, 2013) and laboratory experiments (Finnegan et al., 2007; Johnson & Whipple, 2010) have shown that low sediment supply rates promote vertical erosion and high sediment supply rates promote lateral erosion. Vertical erosion is relatively high when bare exposed bedrock is exposed to sediment impact, but relatively low when the bed is protected by the alluvial cover. Lateral erosion is thought to be high when the bed is alluviated and able to deflect bedload particles into the wall. However, studies of the competition between lateral and vertical erosion due to bedload particle impacts remain qualitative.

Our lateral erosion model replicates the essential lateral erosion patterns that were observed in the Fuller Experiments by explicitly accounting for bedrock erosion from bedload particle impacts. We couple the lateral erosion model with a vertical erosion model to quantify the changes in vertical and lateral erosion due to impacts from bedload particles for a range of hydraulic and sediment transport conditions. We generalize the lateral erosion model by treating the roughness elements as alluvial cover that has the same grain size as the bedload particles ($D_r = D$) and use a nondimensional form of the model to show that for a given grain size the full model behavior collapses to a unique functional surface in the parameter space defined by two nondimensional quantities: the relative sediment supply (q_s/q_t) and the transport stage (τ_s^*/τ_c^*). We then combine the lateral erosion model with the Sklar & Dietrich (2004) vertical erosion model and quantify the competition between lateral and vertical erosion by looking at the ratio of lateral to vertical erosion rate as a function of relative sediment supply (q_s/q_t) and the transport stage (τ_s^*/τ_c^*).

672 *5.1 Nondimensional framework of coupled numerical model*

673 The nondimensional framework for the lateral erosion model is intended to explore the
674 variation of instantaneous lateral erosion rate for the given hydraulic and transport conditions,
675 rather than the co-evolution of lateral erosion rate, wall morphology and shear stress over
676 time. We start by determining the size and distribution of roughness elements on the bed.
677 Assuming the alluvial cover provides the only roughness elements capable of deflecting
678 bedload particles, and has the same size as the bedload particles ($D_r = D$), the fraction of
679 roughness elements F_r increases with sediment supply rate and can be calculated from the
680 relative sediment supply q_s/q_t using the method proposed by Sklar & Dietrich (2004)

681 $$F_r = \frac{q_s}{q_t} \tag{43}$$

682 where the fraction of roughness elements (alluvial cover) F_r is assumed to be a linear function
683 of relative sediment supply, and the transport capacity q_t can be estimated from the
684 Fernandez Luque & Van Beek (1976) bedload sediment transport relation

685 $$q_t = 5.7\rho_s(R_b g D^3)^{0.5}(\tau_s^* - \tau_c^*)^{1.5} \tag{44}$$

686 where $R_b = \rho_s/\rho_w - 1$ is nondimensional buoyant density. Assuming the alluvial cover is
687 uniformly distributed on the bed, the distance between two adjacent roughness elements d is
688 expressed as

689 $$d = \frac{D}{F_r} \tag{45}$$

690 Substituting equation 43 into equation 45, d can be obtained from the given grain size D and
691 relative sediment supply rate q_s/q_t

692 $$d = D\frac{q_t}{q_s} \tag{46}$$

693 We then determine the initial saltation trajectories and deflection trajectories from discrete
694 roughness elements from equations 9-15, for a given transport stage τ_s^*/τ_c^* and grain size D.
695 These results are then applied in a continuum model by calculating the deflection rates I_c on
696 each cell of the roughness surface from equation 16-25, the impact rate I_w on the wall from
697 I_c, the impact velocities v_i and positions on the wall from equation 26-28 and the resultant
698 total erosion rates E_t for all impact locations on the wall from combining equations 32-35 for
699 the given rock parameters (k_v, σ_T and Y), relative sediment supply rate q_s/q_t, transport stage
700 τ_s^*/τ_c^* and grain size D

701 $$E_t = \sum \frac{\pi\rho_s D^3 v_i^2 Y}{6k_v\sigma_T^2} I_w. \tag{47}$$

702 The downstream velocity after deflection in equation 26 is assumed to be constant here for
703 simplification, without considering the variation of deflection trajectories in the longitudinal
704 direction. To account for the transition from bedload to suspension that is equivalent to a
705 particle taking a hop of infinite length, Sklar & Dietrich (2004) assume that the impact rate
706 on the bed and the impact velocity become negligible as u^* approaches w_f (see their equation
707 21 and 22). When l_s becomes infinite in our lateral erosion model, the impact velocity on the
708 bed w_s (equation 12) before deflection, and hence the impact velocity on the wall v_i
709 (equation 33) monotonically increases with higher transport stage. This is problematic

because the lateral erosion rate should decline as the transport stage approaches the suspension threshold. To keep the lateral erosion model consistent with the Sklar & Dietrich (2004) vertical erosion model, v_i is set to be negligible by multiplying it with $(1-(u^*/w_f)^2)^{0.5}$ in equation 47 as u^* approaches w_f and rearranging equation 47

$$E_t = \frac{\pi \rho_s D^3 Y}{6 k_v \sigma_T^2}(1-(u^*/w_f)^2)\sum(v_i^2 I_w). \quad (48)$$

To evaluate the average lateral erosion rate E_l on the wall, E_t is averaged over the maximum impact elevation on the wall z_{lmax} which is obtained from the distribution of z_l of all deflection trajectories on the wall

$$E_l = \frac{\pi \rho_s D^3 Y}{6 k_v \sigma_T^2}\frac{(1-(u^*/w_f)^2)}{dz_{lmax}}\sum(v_i^2 I_w) \quad (49)$$

The variable u^*/w_f is a function of transport stage τ_s^*/τ_c^* for a given grain size D, so E_l is a function of four variables, including rock parameters (σ_T and Y), relative sediment supply rate q_s/q_t, transport stage τ_g^*/τ_c^* and grain size D. The influence of rock parameters (σ_T and Y) in equation 49 can be erased when E_l is non-dimensionalized as (Sklar & Dietrich, 2004)

$$E_l^* = \frac{E_l \sigma_T^2}{\rho_s Y (gD)^{1.5}} = \frac{\pi (D/g)^{1.5}}{6 k_v}\frac{(1-(u^*/w_f)^2)}{dz_{lmax}}\sum(v_i^2 I_w) \quad (50)$$

Therefore, E_l^* can be considered as a function of just two nondimensional quantities, the relative sediment supply q_s/q_t and the transport stage τ_s^*/τ_c^* for a constant grain size D. Meanwhile, an analytical solution for the non-dimensional vertical erosion rate E_v^* has been proposed to be a function of q_s/q_t and τ_s^*/τ_c^* by Sklar & Dietrich (2004)

$$E_v^* = \frac{E_v \sigma_T^2}{\rho_s Y (gD)^{1.5}} = \frac{0.046(R_b \tau_c^*)^{1.5}}{k_v}\frac{q_s}{q_t}(1-\frac{q_s}{q_t})(\frac{\tau_s^*}{\tau_c^*}-1)(1-(\frac{u^*}{w_f})^2)^{1.5} \quad (51)$$

Vertical and lateral erosion can be coupled from the ratio e

$$e = \frac{E_l^*}{E_v^*} \quad (52)$$

because both erosion rates can be related to two variables q_S/q_t and τ_s^*/τ_c^* for a given D.

5.2 Competition between vertical and lateral erosion

In order to explore the competition between vertical and lateral erosion with varied q_S/q_t and τ_s^*/τ_c^*, we assume that channel erosion is disconnected from the hillslopes. The most direct analogue for the coupled model here is a bedrock canyon or gorge that is deeply incised into a river valley and largely disconnected from the hillslopes. In order to implement lateral and vertical erosion in a coupled format, we must specify various parameters, including the grain-size of transported material, transport thresholds and various sediment, rock and water properties. For convenience, we use values reported by Sklar & Dietrich (2004) for the South Fork Eel River in Northern California (Table 3).

Table 3 Reference site and the model parameter values used as inputs for vertical, lateral and coupled erosion models.

Variable	Value
Bedload particle size D (m)	0.060 [a]
Channel width W (m)	18.0 [a]
Critical Shields stress τ_c^*	0.045 [b]
Water density ρ_w(kg/m^3)	1000 [b]
Sediment density ρ_s (kg/m^3)	2650 [b]
Rock elastic modulus Y (Pa)	5×10^{10} [a]
Dimensionless rock resistance parameter k_v	10^6 [a]
Rock tensile strength σ_T (Pa)	7×10^6 [a]

[a] From Sklar and Dietrich (2004).

[b] Assumed.

The first step in exploring the competition between vertical and lateral erosion involved calculating how E_v^* varies with q_s/q_t and τ_s^*/τ_c^* for the grain size $D = 0.06$ m at the reference site, using the Sklar & Dietrich (2004) model. E_v^* has an analytical solution for q_s/q_t and τ_s^*/τ_c^*, so we can simply determine E_v^* for each combination of q_s/q_t and τ_g^*/τ_c^* from equation 51. Figure 13 shows that E_v^* collapses to a unique functional surface in the parameter space created by q_s/q_t and τ_s^*/τ_c^*. As in Sklar & Dietrich (2004), E_v^* goes to zero at the threshold of motion and suspension along the τ_s^*/τ_c^* axis, and the threshold of full cover and no cover along the q_s/q_t axis. The decline in erosion rate at the threshold for suspension is adopted for simplicity here, but we recognize that this is not strictly correct and that there is some reduced bedrock erosion beyond the suspension threshold (Lamb et al., 2008; Scheingross et al., 2014). E_v^* peaks at the intermediate transport stages (Figure 14a) where the growth in the impact energy is balanced by a decline in the impact frequency as the saltation hop length increases with shear stress, and at moderate relative sediment supply (Figure 14b), where the growth in impact rate is balanced by the reduction in the extent of bedrock exposure with increasing sediment supply.

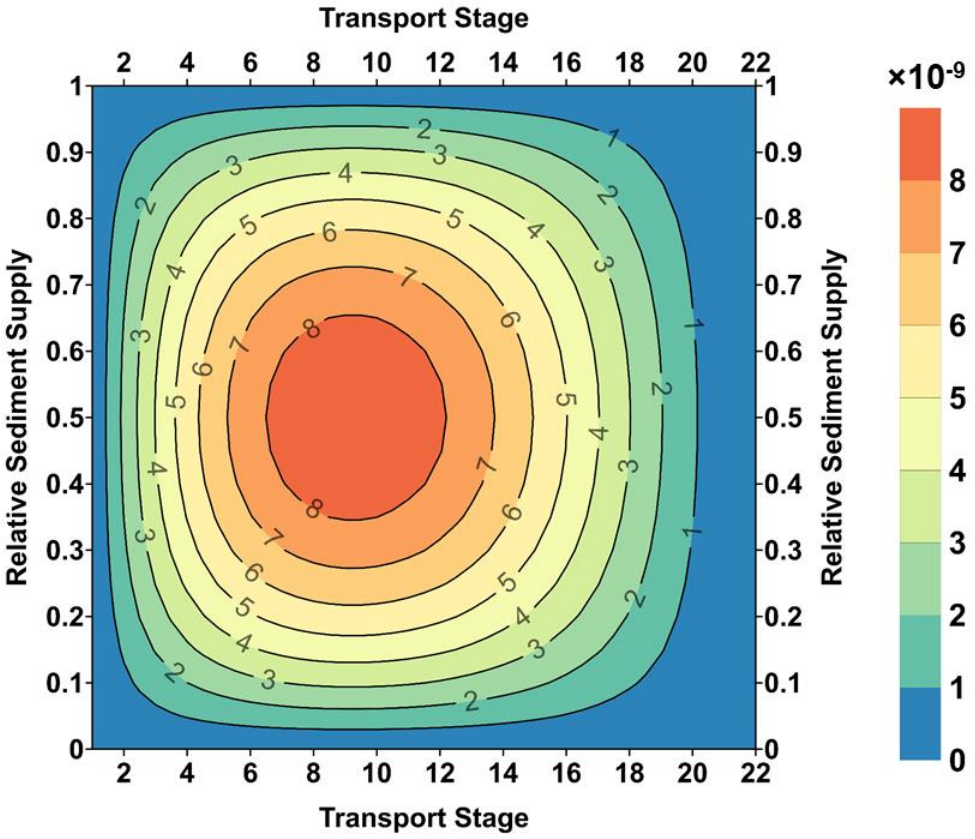

Figure 13 Non-dimensional vertical erosion rate (E_v^*) as a function of transport stage and relative sediment supply.

The second step in examining the competition between vertical and lateral erosion was to explore how E_l^* varies with q_s/q_t and τ_s^*/τ_c^* for the grain size D = 0.06 m at the reference site. We varied τ_s^*/τ_c^* from 1 to 22, and for each value of τ_s^*/τ_c^* calculated the initial saltation trajectories (equations 9-12) before deflection by roughness elements and the transport capacity q_t (equation 44). We also varied q_s/q_t from 0 to 1, and for each value of q_s/q_t calculated the distance between two adjacent roughness elements d (equation 46). For each combination of q_s/q_t and τ_s^*/τ_c^* , we calculated the sediment supply rate q_s (equation 43) and used the deflection model to get all the possible individual deflection trajectories from discrete parts of the roughness elements (equations 13-15). We then applied these results in the continuum model by calculating the deflection rates on each cell of the roughness surface (equation 16-25), the maximum erosion height z_{lmax} (equation 26-28), and the resultant E_l (equation 49) and E_l^* (equation 50). Using this nondimensional framework, the lateral erosion model also collapses to the unique functional surface in the parameter space defined by q_s/q_t and τ_s^*/τ_c^* (Figure 15).

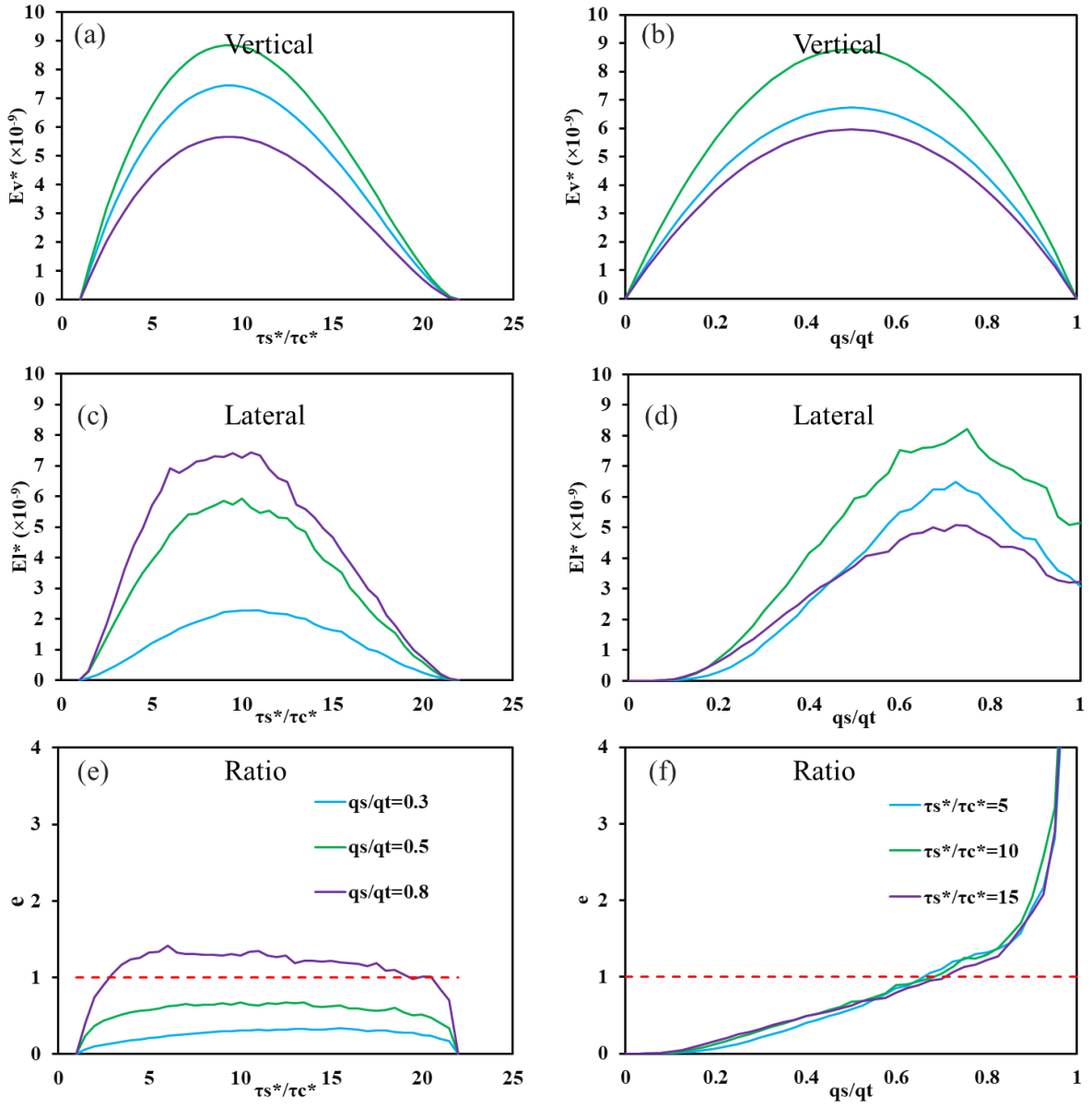

Figure 14 Non-dimensional vertical erosion rate as a function of a) transport stage τ_s^*/τ_c^* and b) relative sediment supply q_s/q_t; non-dimensional lateral erosion rate as a function of c) transport stage τ_s^*/τ_c^* and d) relative sediment supply q_s/q_t,and the ratio of lateral to vertical erosion rate as a function of e) transport stage τ_s^*/τ_c^* and f) relative sediment supply q_s/q_t.

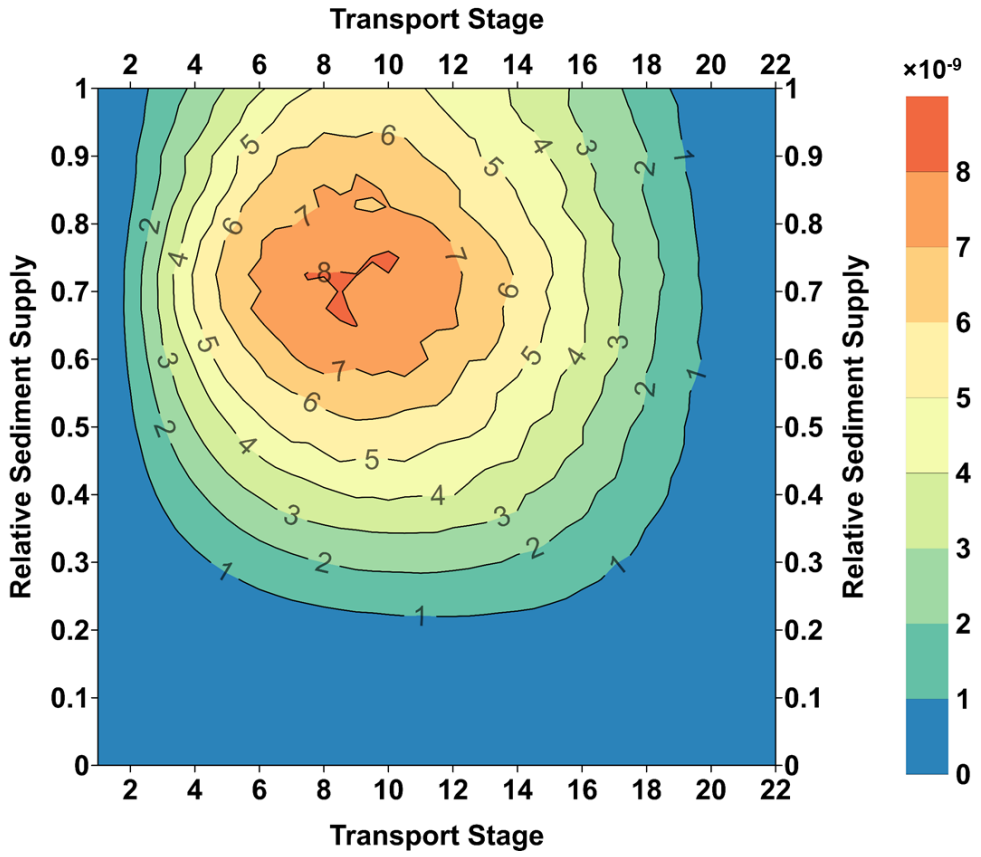

Figure 15 Non-dimensional lateral erosion rate (E_l^*) as a function of transport stage and relative sediment supply.

Figure 15 reveals that E_l^* goes to zero at the threshold of motion and suspension along the τ_s^*/τ_c^* axis, and the threshold of no cover along the q_s/q_t axis, but is relatively high at the threshold of full cover. As with E_v^*, E_l^* peaks at an intermediate transport stages, however, E_l^* peaks at high relative sediment supply rate (~ 0.7; Figure 15). Figure 14c-d illustrates the pattern of E_l^* with increasing shear stress and relative sediment supply rate more clearly. E_l^* shows a parabolic variation with transport stage, where E_l^* is zero at the threshold of motion due to a lack of particle movement along the transport stage axis (Figure 14c). As the transport stage exceeds the threshold for motion, E_l^* increases gradually with transport stage due to the growth in impact velocity. However, the impact frequency of bedload particles on the roughness element decreases with transport stage, because the saltation trajectories tend to grow more elongated with increasing shear stress. The growth in the particle impact energy and the reduction in the impact frequency with increasing shear stress results in a peak E_l^* at intermediate transport stages. E_l^* goes to zero at the threshold of suspension, because no impacts between roughness elements and bedload particles occur in our model. This is an artifact of the saltation model used. Some limited lateral erosion is possible from deflected particles above the suspension threshold, but E_l^* would be low. Along the relative sediment supply axis, a parabolic variation of E_l^* also exists. E_l^* is zero when the bed is free of cover and remains negligible when the relative sediment supply is <0.15 (Figure 14d). This occurs because when the relative sediment supply is low, the fraction of bed coverage is low, and there are relatively few deflectors on the bed. E_l^* gradually grows with the relative sediment supply rate above 0.15 due to the increase of the number of saltating bedload particles and the

extent of roughness. However, E_l^* peaks at the relative sediment supply of ~ 0.7 (Figure 14d) due to a competition between the impact area A_c and wall-normal velocity v_o and the number of deflections on each cell of the roughness surface. When q_s/q_t increases, the distance between two adjacent roughness elements starts to decline, which will reduce the deflections near the bottom of the roughness surface and force bedload particles to impact near the top of the roughness surface. The concentration of impacts near the top of the roughness surface will lead to lower impact area on each cell as the cell starts to get close to the flux surface (Figure 5) and lower wall-normal velocity v_o after deflection by the cell as the vertical velocity w_s before deflection declines and the normal vector increasingly points upward. However, the number of deflections on each cell increases with higher sediment supply rates as q_s/q_t increases. The decrease in impact area A_c and wall-normal velocity v_o and the increase of the number of deflections on each cell of the roughness surface with higher q_s/q_t will lead to a peak in E_l^* when they are balanced. E_l^* starts to decline for q_s/q_t above ~ 0.7 and is ~ 75% of the peak lateral erosion rate at the threshold of full cover.

The contour lines of non-dimensional lateral erosion rate are not smooth. This is not improved by using smaller time steps and space grids. The roughness element surface is discretized into nearly uniform triangular grid cells to model the collision with a finite number of bedload particles, which leads to variations in the modelled erosion rate. Some variation is also caused by our numerical approach. We track the movement of each particle to obtain the impact velocity and the impact position on the wall under every combination of relative sediment supply rate and transport stage instead of deriving explicit empirical correlations, resulting in a lateral erosion model that varies irregularly with control variables.

The competition between vertical and lateral erosion was calculated from the ratio of E_l^* to E_v^* for each combination of q_s/q_t and τ_s^*/τ_c^*. The ratio e collapses to a unique functional surface in the parameter space created by q_s/q_t and τ_s^*/τ_c^* (Figure 16). e goes to zero with no bed cover, at the thresholds of motion and suspension, and is infinite when the bed has full cover. Figure 14e-f illustrates the patterns in e with changes of τ_s^*/τ_c^* and q_s/q_t. Along the τ_s^*/τ_c^* axis, e is parabolic, with a peak at an intermediate transport stage. This occurs because E_l^* increases more rapidly than E_v^* at lower transport stages (<10), and decreases more rapidly than E_v^* at high transport stages (Figure 14a-b), for a constant q_s/q_t. In contrast, e shows a monotonic increase with increasing q_s/q_t (Figure 14f); e goes to zero when q_s/q_t = 0 and gradually increases with relative q_s/q_t (> 0.15), because E_l^* grows faster than E_v^* when the relative sediment supply rate is below 0.5, and E_l^* continues to increase but E_v^* start to decrease when the relative sediment supply is between 0.5 and 0.7 (Figure 14b and d). The ratio e continues to increase at high relative sediment supply (> 0.7), because E_l^* decreases more slowly than E_v^*. When the bed is fully covered, the ratio goes to infinity as the lateral erosion rate is relatively high, but the vertical erosion rate goes to zero.

The coupled model shows that the lateral erosion rate is lower than the vertical erosion rate under nearly 75% of the transport and supply conditions (Figure 16). Lateral erosion is negligible at low sediment supply rates when the bed coverage is less than 20% and gradually increases with the extent of alluvial cover, but only dominates at high sediment supply rates when the bed is largely covered by roughness elements. The ratio e is ultimately controlled by the change in E_v^* and E_l^* and where it is high does not necessarily correspond to where

either E_v^* or E_l^* are largest. Nevertheless, lateral erosion only dominates over vertical erosion under a limited range of conditions.

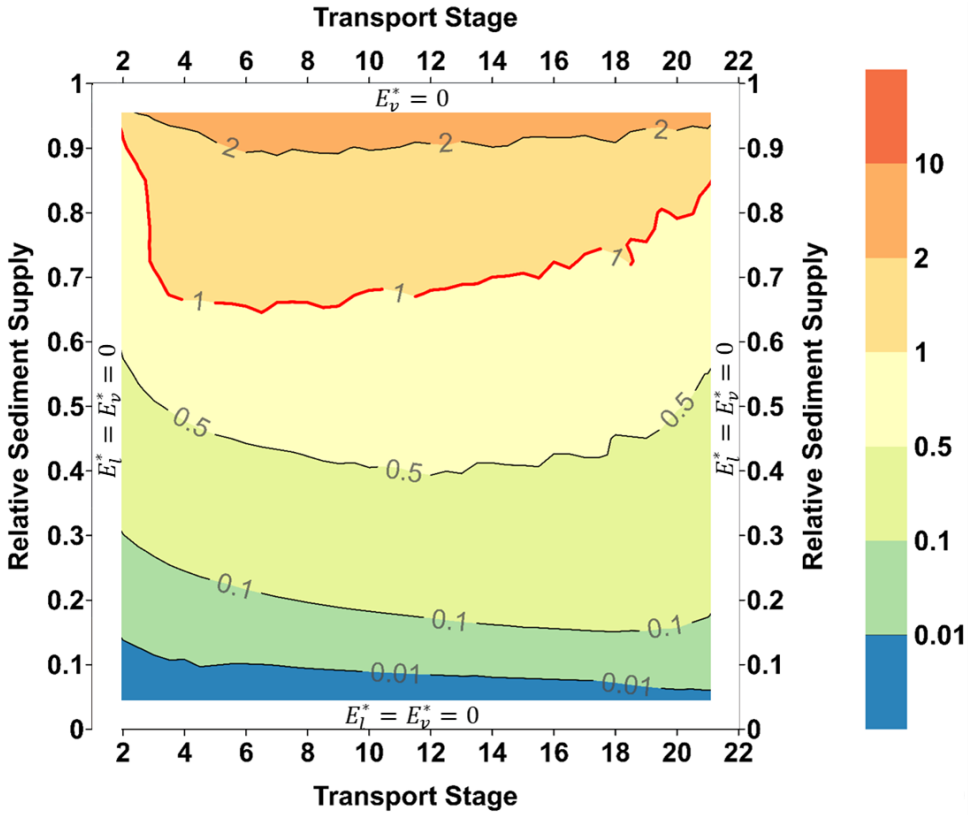

Figure 16 The ratio of lateral to vertical erosion rate $e = E_l^*/E_v^*$ as a function of transport stage and relative sediment supply.

6. Discussion

The lateral erosion model confirms that bedload particle impact is a viable mechanism for lateral erosion in bedrock rivers by reproducing key patterns in lateral erosion from the Fuller Experiments, including the undercut wall shape, the peak erosion rate and the total erosion rate. Saltating bedload particles obtain lateral momentum to erode the wall by colliding with the roughness elements on the bed. The bedload particle impacts concentrate in a zone near the bottom of the walls, thereby creating an undercut wall shape.

6.1 Limiting conditions on lateral erosion

While our model can reproduce key features of lateral rock erosion in channels, it is useful to consider some limiting conditions on the process of lateral erosion by abrasion. Before doing so, it is useful to acknowledge that the lateral erosion model predicts instantaneous erosion rates. Application of the model to a natural channel needs to consider time scales of effectiveness for both the vertical and lateral erosion processes, which are ultimately controlled by discharge and sediment supply variations (Lague et al., 2005, 2010; Finnegan et al., 2005; Finnegan & Balco, 2013; Inoue et al., 2014, 2016). Wall erosion is the integrated result of intermittent periods of variable discharge and sediment supply. Nevertheless, during periods when wall erosion can be effective, there are limits to how far lateral erosion by abrasion may occur before one of the following happens: 1) changes in channel geometry cause the stress to fall below the threshold of motion to maintain bedload; 2) the undercut becomes so deep that deflected particles can no longer reach the wall; or 3) the undercut is so deep that the rock mass above it fails into the channel (as in Figure 1a).

As the wall is undercut over time, mean velocity and shear stress drop due to the increase in cross-sectional area. The lateral erosion rate will go to zero when the shear stress is below the threshold for particle motion. However, this is unlikely to happen because the stress and wall morphology co-evolve. At low stresses, where changes in the wall would affect the shear stress, the erosion rate would be low, so the wall evolution would be very slow. It would therefore take an excessively long time for the shear stress to drop below the threshold of motion.

The lateral momentum for bedload particles to reach the wall drops due to the increase in travel distance as the wall gets undercut over time. We select the 10.0 mm roughness section as an example and ran the lateral erosion model over 15 hr. The lateral erosion stops after 12 hr, although the transport stage (~2.5) at the end of the time period is still enough to transport bedload particles (Figure 17). This occurs because the wall is eroded over 18 mm at the end of the time period, which is too far for bedload particles to impact on the wall at transport stage of ~2.5. As such, the increase in travel distance provides a greater limiting condition on lateral erosion than the drop of shear stress. Using a constant resistance coefficient over the run may overpredict the shear stress because the hydraulic roughness may increase as the wall is undercut. Also, the calculation shown in Figure 17 does not include any roughness elements within the undercut. If the newly exposed bed by channel undercutting becomes alluviated, those deflectors would allow lateral erosion to continue.

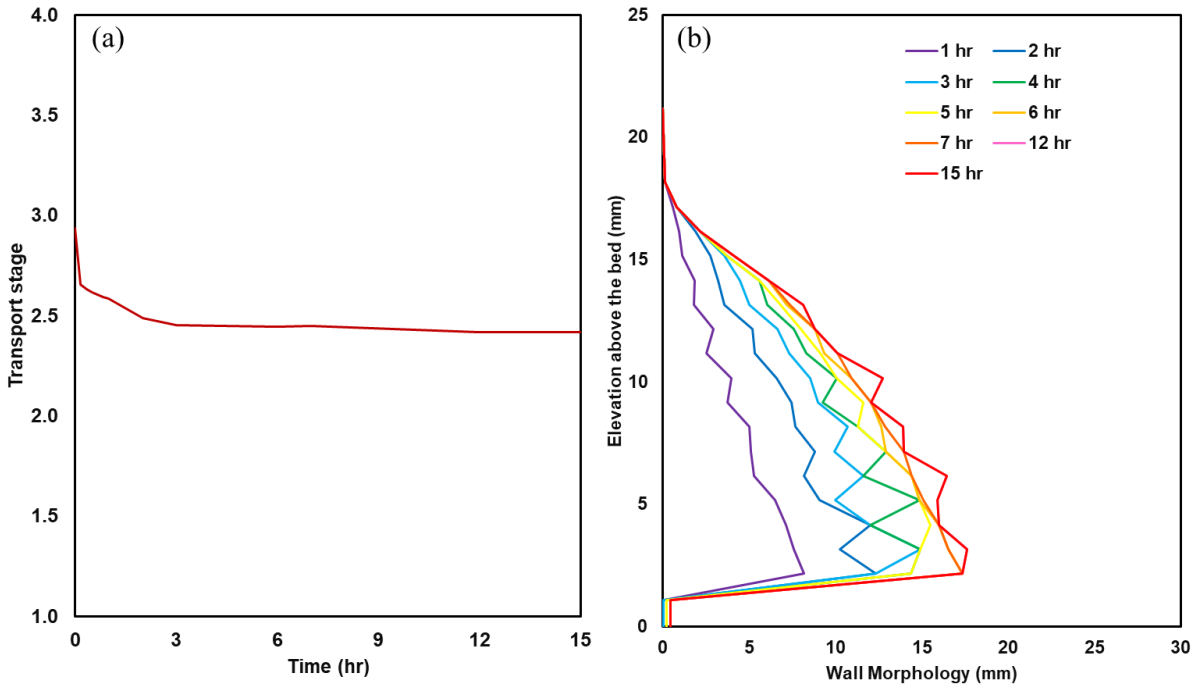

Figure 17 a) Shear stress evolution and b) wall morphology of 10.0 mm roughness section (C2) over 15 hr.

Continued undercutting of the lower wall creates an imbalance on the wall and may cause the upper part to collapse and to widen the whole channel. Such a mechanism of channel widening has been documented in both experiments (Carter & Anderson, 2006) and field data (Cook et al., 2014). However, the question of how far the wall needs to be undercut before it fails remains unanswered. Bedrock walls with lesser rock mass strength can fail more easily as the lower part of the wall is undercut. The degree of fracturing and jointing on the bedrock walls influences the rate of rock sliding and toppling and hence channel width. Bedrock bedding may play a dominant role in controlling the wall collapse. Undercut bedrock walls with vertical bedding can cause a channel to widen more effectively than with horizontal bedding, which may remain intact for deeper undercuts.

6.2 Undercut wall shape dynamics and channel cross-section shape

In bedrock channels with a planar bed, the competition between vertical and lateral erosion is controlled by the extent of alluvial cover under different sediment supply conditions, which may lead to different wall shapes. In a low sediment supply environment, the channel bed is more exposed and vertical erosion will dominate, with lateral erosion relatively negligible, resulting in a near straight wall shape. At an intermediate to high sediment supply where the bed is 50%-90% covered, both the bed and walls can be cut by bedload particle impacts. The continuing lowering of the channel bed will shift down the lateral erosion zone by preventing the bedload particles impacting on a fixed elevation on the walls. This will create an undercut wall shape that keeps the same width but spreads more deeply over time. However, when the bed is near fully covered (>90%), the bed is relatively static due to the protection of alluvium,

leading to an undercut wall shape that gets wider over time. As such, the wall shape would change from near straight to deeply undercut as the sediment supply increases.

However, the undercut wall shape may be modified by roughness elements made of the bedrock surface. The beds of bedrock rivers are mostly marked by a wide range of sculpted bed morphologies (Wohl, 1993; Montgomery & Buffington, 1997; Wohl & Merritt, 2001; Richardson & Carling, 2005), such as potholes, flutes, furrows, runnels, etc. In a bedrock channel with bedrock obstacles near the walls, bedload particles can be deflected toward the walls by bedrock obstacles even when no alluvial cover exists. Beer et al. (2017) mapped the lateral erosion patterns in a bedrock gorge in the Swiss Alps under three bedrock obstacle conditions: 1) no bedrock obstacle; 2) low bedrock obstacle; 3) high bedrock obstacle. Although the magnitude of lateral erosion on the bedrock walls was nearly the same over three conditions, the undercut wall shape was more elevated in sections with low and high bedrock obstacle and more irregular in sections with low bedrock obstacle. The occurrence of bedrock obstacles to deflect bedload particles to higher elevations than the alluvium may have the effect of elevating the undercut zone. The size of bedrock roughness obstacles can influence the erosion rate from two opposite effects. Small bedrock obstacles do not have large surface area to deflect bedload particles but tend to have high impact velocity due to low form drag. Larger bedrock obstacles have more surface area for deflections, but the impact velocity will be reduced because of higher form drag. This may explain the near same lateral erosion rate in bedrock rivers with no, low and high bedrock obstacle observed by Beer et al. (2017). Intermediate bedrock obstacle that balances the tradeoff between surface area and impact velocity may be most beneficial for lateral erosion.

It is possible to infer the relative width to depth ratio and degree of incision of a channel cross-section from Figure 16. A bedrock channel with a high sediment supply rate, which can be found near the upper corner of Figure 16, is mostly covered by alluvium. This channel would be dominated by lateral erosion with negligible vertical erosion, allowing for a wide bedrock channel, relative to its depth. In contrast, a channel that receives relatively little sediment supply should plot near the lower corner of Figure 16, will preferentially incise the bed and have a lower relative width to depth ratio. Of course, the sediment supply and transport stage conditions of bedrock rivers change over time with hydrographs and sedigraphs in a basin. The ultimate shape of a channel is determined by how long it spends in particular positions on Figure 16. A channel that spends the vast majority of its time in the lower corner of Figure 16 is likely to be narrow and deeply incised. A channel that is in the upper corner of Figure 16 most of the time will be relatively wider. Tracking a channel through time on Figure 16 requires a full morphodynamic implementation of the model presented herein, which requires imposed hydrographs and sedigraphs.

6.3 Model limitations and further prospects

There are a number of simplifications in our model, which were necessary to produce a result, that may affect the outcomes. Our model uses a uniform grain size with spherical shape for sediment particles to represent the wide distribution of grain sizes supplied to bedrock rivers. Grain size controls the threshold for motion and hence the transport stage, and hence impact velocity and impact rates. Grain size of the alluvial cover determines the elevation of collision, thereby influencing the transfer of momentum during collision and the

971 impact height on the wall. High points of the alluvial cover that protrude above the reach of
972 bedload abrasion are not effective in deflecting bedload particles into the wall. Therefore, the
973 distribution of grain sizes supplied by the upstream catchment (Sklar et al., 2017) may
974 influence the lateral erosion rate by changing the fraction of total load that is transported as
975 bedload and the momentum transfer of bedload particles during collision with the alluvial
976 cover. The shape of sediment particles determines the distribution of impact angles during
977 collision between roughness elements and bedload particles, thereby influencing the direction
978 of movement after collision. Given that our assumption of a uniform grain size with spherical
979 shape has well reproduced the erosion patterns observed in the Fuller Experiments, which
980 used non-spherical deflectors, the influence of the non-spherical shapes of natural particles on
981 lateral erosion rate may be negligible.

982 Our lateral erosion model uses numerical formulations to track the movement of individual
983 bedload particles. The potential for bedrock erosion by bedload impacts at transport stages
984 above the suspension threshold are ignored. It is possible that particle impacts might be
985 viscously damped for fine grains that are transported as suspended load. Yet, bedload
986 transport remains a significant, but decreasingly important component of the total load as
987 transport stages increase above the suspension threshold (Lamb et al., 2008; Scheingross et
988 al., 2014). The suspended load has been proposed to be responsible for lateral erosion
989 through turbulent fluctuations that laterally sweep particles to impact on the wall (Whipple et
990 al., 2000). Nonetheless, it is not possible for us to track particle movements above the
991 suspension threshold, so we force the lateral erosion rate to zero at the suspension threshold,
992 which is consistent with the Sklar & Dietrich (2004) vertical erosion model.

993 Another simplification in the lateral erosion model is our assumption that bedload particles
994 are uniformly transported in a rectangular channel with a planar bed and straight walls. In a
995 rectangular bedrock channel, the shear stress is higher in the channel center than near the wall
996 due to the wall drag (Parker, 1978). This flow structure results in faster bedload particle
997 velocity in the center than near the walls. Bedload particles have also been observed to
998 preferentially move in the channel center (Finnegan et al., 2007; Nelson & Seminara, 2011).
999 The higher speed and greater concentration of bedload particles in the channel center will
1000 increase the impact energy and frequency and accelerate the vertical erosion rate in the
1001 channel center, but slow down the lateral erosion rate due to the increasing travel distance for
1002 the particles to impact on the wall.

1003 The simplified treatment of flow dynamics in the model may influence the result as well. The
1004 movement of sediment after collision is modelled by assuming that the influence of
1005 turbulence on trajectories is negligible. However, local turbulent fluctuations can be intense
1006 above a bed with significant roughness (Richardson & Carling, 2005). We assume that flow
1007 advection is negligible near the bed so that particles impact on roughness elements and
1008 subsequently on the wall without being swept away with the flow. The advective component
1009 of the impact velocity can be significant over roughness elements (Tinkler, 1997; Johnson &
1010 Whipple, 2007), where flow goes around large roughness elements and advects the sediment
1011 toward the wall, potentially increasing the impact velocity and rates on the wall. Non-uniform
1012 flow in deeply incised bedrock rivers may exacerbate this problem. Erosion rate scales with
1013 the impact velocity squared, so erosion is controlled by local velocity. Venditti et al. (2014)
1014 documented plunging flow structures, compensated by upwelling of highly turbulent, low-
1015 velocity fluid along the walls as flow entered a narrow and deep canyon reach. These

secondary flow cells can direct bedload particles to the walls without being deflected by the roughness element, which may enhance undercutting.

The inherent limitation of the model is that it requires discretizing roughness elements and tracking the movement of individual bedload particles, which makes it difficult to test the sensitivity of lateral erosion rate on changes of variables in bedrock channels, such as discharge, sediment supply, grain size, shear stress, rock strength and bed roughness, and to predict bedrock channel dynamics at reach or larger scales with varied discharge and sediment supply over time. An analytical solution for the lateral erosion model may exist and can be further developed to explore the complex dynamics in bedrock channels if the impact angle on the roughness element is fixed as 45 degrees relative to the base of the roughness element head instead of discretizing the roughness elements, because the lateral erosion is dominated by the impacts here (Figure 5 and Figure 7).

Despite these simplifications, our model agrees well with experiments that have relatively simple geometries (Fuller et al., 2016), which suggests that the model captures the fundamental mechanism correctly. Furthermore, the model generates some features that are qualitatively similar to field observations (Cook et al., 2014; Beer et al., 2017). Nevertheless, some caution should be exercised in applying the model where the transport stages exceed the suspension threshold, where the cross-section is irregular, or where the flow field is non-uniform.

6. Conclusion

We have developed a mechanistic model for lateral erosion of bedrock channel banks by bedload particle impacts using well established empirical relations for initial velocities of bedload particles, a simplified reflection methodology for collision with roughness elements, and a numerical model for tracking the motion of bedload particles from collision to impacts on the wall. Simulations of the Fuller Experiments show that the model successfully predicts the essential undercut wall shape, the dynamics of peak erosion rate and total cross-sectional erosion rate with roughness element size, which not only validates the formulation of our lateral erosion model but also supports the bedload particle impacts as an effective mechanism for lateral incision in bedrock rivers. The predicted lateral erosion rate can be further expressed in non-dimensional form as a function of transport stage and relative sediment supply for the given grain size by assuming that the alluvial cover due to deposition of sediment particles is effective at deflecting downstream transport particles. The non-dimensional lateral erosion model defines a unique functional surface bounded by four thresholds, including the threshold of motion, the threshold of suspension, the threshold of no cover, and the threshold of full cover. The lateral erosion is relatively high at the threshold of full cover, but turns to be zero at all other three thresholds. The model also predicts a peak lateral erosion rate when the bed is near 70% covered, due to a trade-off of deflection rates and deflection angles as the sediment supply increases. A coupled model that combines vertical erosion with lateral erosion due to bedload particle impacts is further developed. The coupled model predicts that vertical erosion dominates under ~ 75% of transport and supply conditions on the unique functional surface. The lateral erosion only outpaces the vertical erosion when the bed is near fully covered.

Acknowledgments

The work was supported by the Natural Science and Engineering Research Council of Canada Discovery (NSERC) Grants to J.V. We thank Mike Church and Gwenn Flowers for comments on an earlier draft. The Matlab code for the model is available here: https://vault.sfu.ca/index.php/s/Jl5a8gOerxscWQf.

References

Anderson, R. S. (1994). Evolution of the Santa Cruz Mountains, California, through tectonic growth and geomorphic decay. *Journal of Geophysical Research: Solid Earth*, *99*(B10), 20161–20179. https://doi.org/10.1029/94JB00713

Beer, A. R., & Turowski, J. M. (2015). Bedload transport controls bedrock erosion under sediment-starved conditions. *Earth Surface Dynamics*, *3*(3), 291–309. https://doi.org/10.5194/esurf-3-291-2015

Beer, Alexander R., Turowski, J. M., & Kirchner, J. W. (2017). Spatial patterns of erosion in a bedrock gorge. *Journal of Geophysical Research: Earth Surface*, *122*(1), 191–214. https://doi.org/10.1002/2016JF003850

Carter, C. L., & Anderson, R. S. (2006). Fluvial erosion of physically modeled abrasion-dominated slot canyons. *Geomorphology*, *81*(1–2), 89–113. https://doi.org/10.1016/J.GEOMORPH.2006.04.006

Chatanantavet, P., & Parker, G. (2009). Physically based modeling of bedrock incision by abrasion, plucking, and macroabrasion. *Journal of Geophysical Research*, *114*(F4), F04018. https://doi.org/10.1029/2008JF001044

Cook, K. L., Turowski, J. M., & Hovius, N. (2014). River gorge eradication by downstream sweep erosion. *Nature Geoscience*, *7*(9), 682–686. https://doi.org/10.1038/ngeo2224

Cundall, P. A., & Strack, O. D. L. (1979). Discrete Numerical Model for Granualr Assemblies. *Geotechnique*, *29*(1), 47–65. https://doi.org/10.1680/geot.1979.29.1.47

Davis, R. H., Serayssol, J.-M., & Hinch, E. J. (1986). The elastohydrodynamic collision of two spheres. *Journal of Fluid Mechanics*, *163*(1), 479. https://doi.org/10.1017/S0022112086002392

Dietrich, W. E. (1982). Settling velocity of natural particles. *Water Resources Research*, *18*(6), 1615–1626. https://doi.org/10.1029/WR018i006p01615

Egholm, D. L., Knudsen, M. F., & Sandiford, M. (2013). Lifespan of mountain ranges scaled by feedbacks between landsliding and erosion by rivers. *Nature*, *498*(7455), 475–478. https://doi.org/10.1038/nature12218

Ferguson, R. I., Hardy, R. J., & Hodge, R. A. (2019). Flow resistance and hydraulic geometry in bedrock rivers with multiple roughness length scales. *Earth Surface Processes and Landforms*, *44*(12), 2437–2449. https://doi.org/10.1002/esp.4673

Fernandez Luque, R., & Van Beek, R. (1976). Erosion And Transport Of Bed-Load Sediment. *Journal of Hydraulic Research*, *14*(2), 127–144. https://doi.org/10.1080/00221687609499677

Finnegan, N. J., & Balco, G. (2013). Sediment supply, base level, braiding, and bedrock river terrace formation: Arroyo Seco, California, USA. *Geological Society of America Bulletin*, *125*(7–8), 1114–1124. https://doi.org/10.1130/B30727.1

Finnegan, Noah J., Roe, G., Montgomery, D. R., & Hallet, B. (2005). Controls on the channel width of rivers: Implications for modeling fluvial incision of bedrock. *Geology*. https://doi.org/10.1130/G21171.1

Finnegan, Noah J., Sklar, L. S., & Fuller, T. K. (2007). Interplay of sediment supply, river

1105 incision, and channel morphology revealed by the transient evolution of an experimental
1106 bedrock channel. *Journal of Geophysical Research: Earth Surface*.
1107 https://doi.org/10.1029/2006JF000569

1108 Fuller, Theodore K., Perg, L. A., Willenbring, J. K., & Lepper, K. (2009). Field evidence for
1109 climate-driven changes in sediment supply leading to strath terrace formation. *Geology*,
1110 *37*(5), 467–470. https://doi.org/10.1130/G25487A.1

1111 Fuller, Theodore K., Gran, K. B., Sklar, L. S., & Paola, C. (2016). Lateral erosion in an
1112 experimental bedrock channel: The influence of bed roughness on erosion by bed load
1113 impacts. *Journal of Geophysical Research: Earth Surface*.
1114 https://doi.org/10.1002/2015JF003728

1115 Gilbert, G. K. (1877). Report on the Geology of the Henry Mountains. *Oxford University*.
1116 https://doi.org/45/11/3914 [pii]\r10.1167/iovs.04-0492

1117 Hancock, G. S., & Anderson, R. S. (2002). Numerical modeling of fluvial strath-terrace
1118 formation in response to oscillating climate. *GSA Bulletin*, *114*(9), 1131–1142.
1119 https://doi.org/10.1130/0016-7606(2002)114<1131:nmofst>2.0.co;2

1120 Hancock, G. S., Small, E. E., & Wobus, C. (2011). Modeling the effects of weathering on
1121 bedrock-floored channel geometry. *Journal of Geophysical Research*, *116*(F3), F03018.
1122 https://doi.org/10.1029/2010JF001908

1123 Hartshorn, K., Hovius, N., Dade, W. B., & Slingerland, R. L. (2002). Climate-driven bedrock
1124 incision in an active mountain belt. *Science*. https://doi.org/10.1126/science.1075078

1125 Howard, A. D., & Kerby, G. (1983). Channel changes in badlands. *Geological Society of*
1126 *America Bulletin*. https://doi.org/10.1130/0016-7606(1983)94<739:CCIB>2.0.CO;2

1127 Howard, Alan D. (1994). A detachment-limited model of drainage basin evolution. *Water*
1128 *Resources Research*. https://doi.org/10.1029/94WR00757

1129 Huda, S. A., & Small, E. E. (2014). Modeling the effects of bed topography on fluvial
1130 bedrock erosion by saltating bed load. *Journal of Geophysical Research: Earth Surface*,
1131 *119*(6), 1222–1239. https://doi.org/10.1002/2013JF002872

1132 Inoue, T., Iwasaki, T., Parker, G., Shimizu, Y., Izumi, N., Stark, C. P., & Funaki, J. (2016).
1133 Numerical simulation of effects of sediment supply on bedrock channel morphology.
1134 *Journal of Hydraulic Engineering*, *142*(7). https://doi.org/10.1061/(ASCE)HY.1943-
1135 7900.0001124

1136 Inoue, Takuya, Izumi, N., Shimizu, Y., & Parker, G. (2014). Interaction among alluvial
1137 cover, bed roughness, and incision rate in purely bedrock and alluvial-bedrock channel.
1138 *Journal of Geophysical Research: Earth Surface*, *119*(10), 2123–2146.
1139 https://doi.org/10.1002/2014JF003133

1140 Johnson, J. P., & Whipple, K. X. (2007). Feedbacks between erosion and sediment transport
1141 in experimental bedrock channels. *Earth Surface Processes and Landforms*, *32*(7),
1142 1048–1062. https://doi.org/10.1002/esp.1471

1143 Johnson, J. P. L. (2014). A surface roughness model for predicting alluvial cover and bed
1144 load transport rate in bedrock channels. *Journal of Geophysical Research: Earth*
1145 *Surface*, *119*(10), 2147–2173. https://doi.org/10.1002/2013JF003000

1146 Johnson, J. P. L., & Whipple, K. X. (2010). Evaluating the controls of shear stress, sediment

supply, alluvial cover, and channel morphology on experimental bedrock incision rate. *Journal of Geophysical Research: Earth Surface*. https://doi.org/10.1029/2009JF001335

Joseph, G. G., & Hunt, M. L. (2004). Oblique particle-wall collisions in a liquid. *Journal of Fluid Mechanics*, (510), 71–93. https://doi.org/10.1017/S002211200400919X

Joseph, G. G., Zenit, R., Hunt, M. L., & Rosenwinkel, A. M. (2001). Particle-wall collisions in a viscous fluid. *Journal of Fluid Mechanics*, *433*, 329–346. https://doi.org/10.1017/S0022112001003470

Lague, D. (2010). Reduction of long-term bedrock incision efficiency by short-term alluvial cover intermittency. *Journal of Geophysical Research: Earth Surface*. https://doi.org/10.1029/2008JF001210

Lague, Dimitri, Hovius, N., & Davy, P. (2005). Discharge, discharge variability, and the bedrock channel profile. *Journal of Geophysical Research: Earth Surface*. https://doi.org/10.1029/2004JF000259

Lamb, M. P., Dietrich, W. E., & Sklar, L. S. (2008). A model for fluvial bedrock incision by impacting suspended and bed load sediment. *Journal of Geophysical Research: Earth Surface*. https://doi.org/10.1029/2007JF000915

Lamb, M. P., Finnegan, N. J., Scheingross, J. S., & Sklar, L. S. (2015). New insights into the mechanics of fluvial bedrock erosion through flume experiments and theory. *Geomorphology*. https://doi.org/10.1016/j.geomorph.2015.03.003

Langston, A. L., & Tucker, G. E. (2018). Developing and exploring a theory for the lateral erosion of bedrock channels for use in landscape evolution models. *Earth Surface Dynamics*, *6*(1), 1–27. https://doi.org/10.5194/esurf-6-1-2018

Larsen, I. J., & Lamb, M. P. (2016). Progressive incision of the Channeled Scablands by outburst floods. *Nature*, *538*(7624), 229–232. https://doi.org/10.1038/nature19817

Meshkova, L. V., Carling, P. A., & Buffin-Bélanger, T. (2012). Nomenclature, Complexity, Semi-Alluvial Channels and Sediment-Flux-Driven Bedrock Erosion. In *Gravel-Bed Rivers: Processes, Tools, Environments*. https://doi.org/10.1002/9781119952497.ch31

Montgomery, D. R., & Buffington, J. M. (1997). Channel-reach morphology in mountain drainage basins. *Bulletin of the Geological Society of America*, *109*(5), 596–611. https://doi.org/10.1130/0016-7606(1997)109<0596:CRMIMD>2.3.CO;2

Nelson, P. A., & Seminara, G. (2011). Modeling the evolution of bedrock channel shape with erosion from saltating bed load. *Geophysical Research Letters*. https://doi.org/10.1029/2011GL048628

Niño, Y., García, M., & Ayala, L. (1994). Gravel saltation: 1. Experiments. *Water Resources Research*, *30*(6), 1907–1914. https://doi.org/10.1029/94WR00533

Parker, G. (1978). Self-formed straight rivers with equilibrium banks and mobile bed. Part 1. The sand-silt river. *Journal of Fluid Mechanics*, *89*(01), 109. https://doi.org/10.1017/S0022112078002499

Perron, J. T., Dietrich, W. E., & Kirchner, J. W. (2008). Controls on the spacing of first-order valleys. *Journal of Geophysical Research: Earth Surface*. https://doi.org/10.1029/2007JF000977

Rennie, C. D., Church, M., & Venditti, J. G. (2018). Rock Control of River Geometry: The Fraser Canyons. *Journal of Geophysical Research: Earth Surface*. https://doi.org/10.1029/2017JF004458

Richardson, K., & Carling, P. A. (2005). A typology of sculpted forms in open bedrock channels. In *Special Paper 392: A typology of sculpted forms in open bedrock channels* (pp. 1–108). Geological Society of America. https://doi.org/10.1130/0-8137-2392-2.1

Scheingross, J. S., Brun, F., Lo, D. Y., Omerdin, K., & Lamb, M. P. (2014). Experimental evidence for fluvial bedrock incision by suspended and bedload sediment. *Geology*. https://doi.org/10.1130/G35432.1

Schmeeckle, M. W., Nelson, J. M., Pitlick, J., & Bennett, J. P. (2001). Interparticle collision of natural sediment grains in water. *Water Resources Research*, *37*(9), 2377–2391. https://doi.org/10.1029/2001WR000531

Seidl, M. A., & Dietrich, W. E. (1992). The Problem of Channel Erosion into Bedrock. *CATENA SUPPLEMENT*. https://doi.org/10.1002/cssc.201301001

Sklar, L. S., & Dietrich, W. E. (2001). Sediment and rock strength controls on river incision into bedrock. *Geology*, *29*(12), 1087. https://doi.org/10.1130/0091-7613(2001)029<1087:SARSCO>2.0.CO;2

Sklar, L. S., & Dietrich, W. E. (2004). A mechanistic model for river incision into bedrock by saltating bed load. *Water Resources Research*. https://doi.org/10.1029/2003WR002496

Sklar, L. S., & Dietrich, W. E. (2006). The role of sediment in controlling steady-state bedrock channel slope: Implications of the saltation-abrasion incision model. *Geomorphology*. https://doi.org/10.1016/j.geomorph.2005.08.019

Sklar, L. S., & Dietrich, W. E. (2008). Implications of the saltation-abrasion bedrock incision model for steady-state river longitudinal profile relief and concavity. *Earth Surface Processes and Landforms*. https://doi.org/10.1002/esp.1689

Sklar, L.S., C.S. Riebe, J.A. Marshall, J. Genetti, S. Leclere, C.E. Lukens, and V. Merces (2017). The problem of predicting the particle size distribution of sediment supplied by hillslopes to rivers, *Geomorphology*, doi:10.1016/j.geomorph.2016.05.005

Snyder, N. P., & Kammer, L. L. (2008). Dynamic adjustments in channel width in response to a forced diversion: Gower Gulch, Death Valley National Park, California. *Geology*, *36*(2), 187–190. https://doi.org/10.1130/G24217A.1

Stark, C. P. (2006). A self-regulating model of bedrock river channel geometry. *Geophysical Research Letters*. https://doi.org/10.1029/2005GL023193

Tanaka, G., & Izumi, N. (2013). The Bedload Transport Rate and Hydraulic Resistance in Bedrock Channels Partly Covered with Gravel. *Journal of Japan Society of Civil Engineers, Ser. B1 (Hydraulic Engineering)*, *69*(4), I_1033-I_1038. https://doi.org/10.2208/jscejhe.69.i_1033

Tinkler, K. J. (1997). Rockbed Wear At A Flow Convergence Zone in Fifteen Mile Creek, Niagara Peninsula, Ontario. *The Journal of Geology*, *105*(2), 263–274. https://doi.org/10.1086/515918

Tucker, G. E., & Slingerland, R. L. (1994). Erosional dynamics, flexural isostasy, and long-lived escarpments: A numerical modeling study. *Journal of Geophysical Research:*

Solid Earth, *99*(B6), 12229–12243. https://doi.org/10.1029/94JB00320

Turowski, Jens M., Lague, D., & Hovius, N. (2007). Cover effect in bedrock abrasion: A new derivation and its implications for the modeling of bedrock channel morphology. *Journal of Geophysical Research*, *112*(F4), F04006. https://doi.org/10.1029/2006JF000697

Turowski, Jens M., Hovius, N., Wilson, A., & Horng, M.-J. (2008a). Hydraulic geometry, river sediment and the definition of bedrock channels. *Geomorphology*, *99*(1–4), 26–38. https://doi.org/10.1016/J.GEOMORPH.2007.10.001

Turowski, Jens M., Hovius, N., Hsieh, M. L., Lague, D., & Chen, M. C. (2008b). Distribution of erosion across bedrock channels. *Earth Surface Processes and Landforms*. https://doi.org/10.1002/esp.1559

Turowski, Jens Martin. (2018). Alluvial cover controlling the width, slope and sinuosity of bedrock channels. *Earth Surface Dynamics*, *6*(1), 29–48. https://doi.org/10.5194/esurf-6-29-2018

Turowski, Jens Martin. (2019). Mass balance, grade, and adjustment timescales in bedrock channels, *Earth Surface Dynamics Discuss.*, in review. https://doi.org/10.5194/esurf-2019-47.

Venditti, J. G., Rennie, C. D., Bomhof, J., Bradley, R. W., Little, M., & Church, M. (2014). Flow in bedrock canyons. *Nature*. https://doi.org/10.1038/nature13779

Venditti, J. G., Li, T., Deal, E., Dingle, E., & Church, M. (2019). Struggles with stream power: Connecting theory across scales. *Geomorphology*, 106817. https://doi.org/10.1016/j.geomorph.2019.07.004

Whipple, K. X., Hancock, G. S., & Anderson, R. S. (2000). River incision into bedrock: Mechanics and relative efficacy of plucking, abrasion, and cavitation. *Bulletin of the Geological Society of America*. https://doi.org/10.1130/0016-7606(2000)112<490:RIIBMA>2.0.CO;2

Whipple, Kelin X. (2004). BEDROCK RIVERS AND THE GEOMORPHOLOGY OF ACTIVE OROGENS. *Annual Review of Earth and Planetary Sciences*. https://doi.org/10.1146/annurev.earth.32.101802.120356

Willett, S. D. (1999). Orogeny and orography: The effects of erosion on the structure of mountain belts. *Journal of Geophysical Research: Solid Earth*. https://doi.org/10.1029/1999JB900248

Wobus, C. W., Tucker, G. E., & Anderson, R. S. (2006). Self-formed bedrock channels. *Geophysical Research Letters*. https://doi.org/10.1029/2006GL027182

Wohl, E. E. (1993). Bedrock channel incision along Piccaninny Creek, Australia. *Journal of Geology*, *101*(6), 749–761. https://doi.org/10.1086/648272

Wohl, E. E., & Merritt, D. M. (2001). Bedrock channel morphology. *Bulletin of the Geological Society of America*, *113*(9), 1205–1212. https://doi.org/10.1130/0016-7606(2001)113<1205:BCM>2.0.CO;2

Yanites, B. J. (2018). The Dynamics of Channel Slope, Width, and Sediment in Actively Eroding Bedrock River Systems. *Journal of Geophysical Research: Earth Surface*. https://doi.org/10.1029/2017JF004405

Notation:

A_c projected area of each grid cell (m^2)

A_w impact area on the wall (m^2)

$A(T)$ wetted area at time period T (m^2)

C_1 gravitational acceleration coefficient (ms^{-2})

C_2 drag deceleration coefficient (ms^{-2})

C_d drag coefficient (dimensionless)

C_r restitution coefficient (dimensionless)

d distance between two adjacent roughness elements (m)

D grain size of bedload particles (m)

D_r grain size of roughness elements (m)

e the ratio of lateral to vertical erosion rate (dimensionless)

E_c instantaneous total erosion rate from one cell (m^3s^{-1})

E_b bulk erosion rate (m^2s^{-1})

E_l lateral erosion rate (ms^{-1})

E_l^* nondimensional lateral erosion rate (ms^{-1})

E_t total erosion rate (m^3s^{-1})

E_v^* nondimensional vertical erosion rate (ms^{-1})

E_z erosion rate at elevation z (ms^{-1})

f total friction factor (dimensionless)

f_a friction factor for alluvium (dimensionless)

f_b friction factor for bedrock surface (dimensionless)

f_r friction factor for roughness element (dimensionless)

F_a fraction of alluvium (dimensionless)

F_r fraction of roughness elements (dimensionless)

g gravity acceleration (ms^{-2})

h water depth

h_c impact elevation on the roughness element (m)

h_s saltation hop height (m)

I_c impact rate on grid cell (s^{-1})

I_p impact rate on the upward trajectory plane ($m^{-2}s^{-1}$)

I_w impact rate on the wall (s^{-1})

$\boldsymbol{i_s}$ incoming saltation velocity vector (ms^{-1})

$\boldsymbol{IL}$ impact position vector (ms^{-1})

$\boldsymbol{IV}$ impact velocity vector (ms^{-1})

k_s hydraulic roughness length scale (m)

k_v Rock resistance coefficient (dimensionless)

l_r the distance between the center of the roughness element and the vertex of the upstream facing part of the successive downstream roughness element (m)

l_s saltation hop length (m)

l_{sd} saltation hop length of the downward trajectory (m)

l_{su} saltation hop length of the upward trajectory (m)

l_u downstream distance of impact position

L length of upward trajectory plane (m)

M mass of bedload particles (kg)

$\hat{\boldsymbol{n}}$ surface normal vector (dimensionless)

N number of grids (dimensionless)

$\boldsymbol{o_s}$ outgoing saltation velocity vector (ms^{-1})

$\boldsymbol{p}$ projection of the incoming velocity vector onto the surface normal vector (ms^{-1})

$P(T)$ wetted perimeter at time period T (m)

q_s sediment supply per unit width ($kgm^{-1}s^{-1}$)

q_t transport capacity per unit width ($kgm^{-1}s^{-1}$)

Q_w water discharge ($m^3\ s^{-1}$)

r semi-circle radius cut along the roughness element (m)

R_b nondimensional buoyant density (dimensionless)

S channel slope (dimensionless)

S_t Stokes number (dimensionless)

u instantaneous downstream velocity (ms^{-1})

u^* shear velocity (ms^{-1})

u_i downstream impact velocity (ms^{-1})

u_o outgoing downstream velocity (ms^{-1})

u_s saltation downstream velocity (ms^{-1})

U_z flow velocity at depth z (ms^{-1})

$U(T)$ flow velocity at time period T (ms^{-1})

v instantaneous lateral velocity (ms^{-1})

1339 v_{min} minimum wall-normal velocity limit (ms^{-1})

1340 v_i lateral impact velocity (ms^{-1})

1341 v_o outgoing lateral velocity (ms^{-1})

1342 v_s saltation lateral velocity (ms^{-1})

1343 V_l volume eroded per particle impact (m^3)

1344 w instantaneous vertical velocity (ms^{-1})

1345 w_0 outgoing vertical velocity (ms^{-1})

1346 w_f fall velocity (ms^{-1})

1347 w_i vertical impact velocity (ms^{-1})

1348 w_s saltation vertical velocity (ms^{-1})

1349 W channel width (m)

1350 x_l downstream impact position (ms^{-1})

1351 y_l lateral impact position (m)

1352 Y Young's modulus of elasticity ($kgm^{-1}s^{-2}$)

1353 z_l vertical impact position (m)

1354 z_{lmax} maximum erosion height on the wall (m)

1355 ρ_s sediment density (kgm^{-3})

1356 ρ_w water density (kgm^{-3})

1357 σ_T Rock tensile strength (Pa)

1358 τ total shear stress (Pa)

1359 τ_s shear stress due to skin friction (Pa)

1360 τ_s^* nondimensional shear stress due to skin friction (dimensionless)

1361 τ_c^* critical shields stress for incipient sediment motion (dimensionless)

1362 ΔT time period (min)

1363 Δt time step (s)

1364 Δz vertical interval on the wall (m)

1365 α angle of the upward trajectory plane (^{o})

1366 β angle of the downward trajectory plane (^{o})

1367 θ central angle of impact (^{o})

1368 θ_d central angle limit at the downstream face of roughness element (^{o})

1369 κ Karman's constant (dimensionless)

1370 ν kinematic viscosity of the fluid (m^2s^{-1})

1371